

# Exclusive photoproduction of light and heavy vector mesons: thresholds to very high energies

Lin Tang (唐淋)<sup>1,2</sup> , Hui-Yu Xing (邢惠瑜)<sup>1,2</sup> ,  
Minghui Ding (丁明慧)<sup>a,1,2</sup> , Craig D. Roberts<sup>b,1,2</sup> 

<sup>1</sup>School of Physics, Nanjing University, Nanjing, Jiangsu 210093, China

<sup>2</sup>Institute for Nonperturbative Physics, Nanjing University, Nanjing, Jiangsu 210093, China

2025 October 08

**Abstract** A reaction model for  $\gamma + p \rightarrow V + p$ ,  $V = \rho^0, \phi, J/\psi, \Upsilon$ , which exposes the quark-antiquark content of the photon in making the transition  $\gamma \rightarrow q\bar{q} + \mathbb{P} \rightarrow V$ , where  $q$  depends on  $V$ , and couples the intermediate  $q\bar{q}$  system to the proton's valence quarks via Pomeron ( $\mathbb{P}$ ) exchange, is used to deliver a unified description of available data – both differential and total cross sections – from near threshold to very high energies,  $W$ , for all the  $V$ -mesons. For the  $\Upsilon$ , this means  $10 \lesssim W/\text{GeV} \lesssim 2000$ . Also provided are predictions for the power-law exponents that are empirically used to characterise the large- $W$  behaviour of the total cross sections and slope parameters characterising the near-threshold differential cross sections. Appealing to notations of vector meson dominance, the latter have been interpreted as vector-meson–proton scattering lengths. The body of results indicate that it is premature to link any  $\gamma + p \rightarrow V + p$  data with, for instance, in-proton gluon distributions, the quantum chromodynamics trace anomaly, or pentaquark production. Further developments in reaction theory and higher precision data are required before the validity of any such links can be assessed.

## 1 Introduction

Exclusive vector-meson photoproduction,

$$\gamma + p \rightarrow V + p, \quad \text{with } V = \rho, \phi, J/\psi, \Upsilon, \quad (1)$$

provides a clean environment to study diffractive scattering from the proton and thereby obtain information about the reaction mechanism and both hadrons involved in the process.

<sup>a</sup>e-mail: mhding@nju.edu.cn

<sup>b</sup>e-mail: cdroberts@nju.edu.cn

Understanding the energy dependence of these cross sections has long challenged theory. Contrary to perturbative quantum chromodynamics (QCD) expectations, which suggest that total cross sections should fall as the center-of-mass energy-squared,  $s = W^2$ , increases, experiments show that such photoproduction cross sections actually rise with  $s$  [1]. This issue was analysed, *e.g.*, in Ref. [2], with the conclusion that the mechanism responsible should correspond to exchange of something that has isospin zero and is even under charge conjugation. Interactions of this kind can be expressed in Regge phenomenology via Pomeron,  $\mathbb{P}$ , exchange, with a trajectory whose intercept  $\alpha_{\mathbb{P}}(0) > 1$ . The QCD character of the Pomeron is widely discussed [3, 4]. It is typically supposed to represent the collective exchange of a family of colourless, crossing-even states, with two-gluon exchange being the leading contributor [5]. Connections with glueball physics are also discussed [6, 7].

With the high-energy behaviour of  $\gamma + p \rightarrow V + p$  described by  $\mathbb{P}$  exchange, it is natural to seek an explanation for the cross section at low-energies and determine whether a unified approach to the entire  $s$ -domain is possible. Both these issues were addressed in Ref. [8], which explored the reaction mechanism depicted in Fig. 1 using phenomenological inputs for the required elements. This approach sees the  $q\bar{q}$  component of the photon, where  $q$  is chosen from the set  $\{q = u/d, s, c, b\}$ , depending on  $V$ , exposed by interaction with the proton via  $\mathbb{P}$ -exchange and then transformed into the on-shell vector meson when sufficient reaction energy is available, *i.e.*, once the threshold energy is exceeded:

$$W_{\text{th}}^V = m_p + m_V. \quad (2)$$

Here  $m_p = 0.939 \text{ GeV}$  is the proton mass and  $m_V$  is that of the vector meson produced.

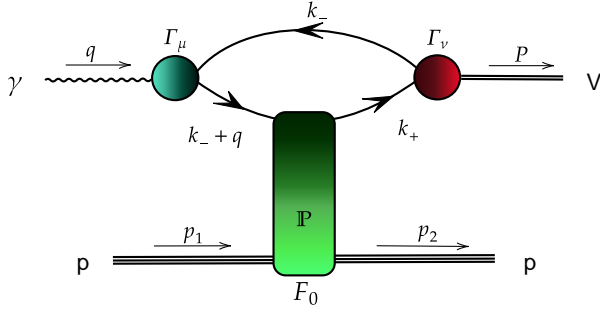


Fig. 1: Reaction model for  $\gamma + p \rightarrow V + p$ , referred to hereafter as  $\mathbb{P}$ -dyn. The quark-antiquark,  $q\bar{q}$ , component of the dressed-photon is probed by Pomeron exchange with the proton, producing an on-shell vector meson,  $V$ . Referring to Eq. (4): the green rectangle describes Pomeron exchange,  $\mathbb{P}$ , including its couplings to the proton and quark – see Sect. 2.2. Further, the solid black curve is  $S_q$ , the dressed  $q$  quark propagator; the shaded lighter-blue circle is  $\Gamma_\mu^\gamma$ , the dressed  $\gamma q\bar{q}$  vertex; and the shaded red circle is  $\Gamma_\nu^V$ , the  $V$ -meson Bethe-Salpeter amplitude – see Sect. 3. Kinematics:  $s = W^2 = -(p_2^2 + P^2)$ ;  $t = -(p_2 - p_1)^2$ .

The  $\gamma \rightarrow q\bar{q} + \mathbb{P} \rightarrow V$  transition matrix element in Fig. 1 can be calculated using QCD propagators and vertices, which may be obtained using either continuum or lattice Schwinger function methods (C[L]SMs). There are three nonperturbative, matrix-valued Schwinger functions; and in the Ref. [9] study of  $\gamma + p \rightarrow J/\psi + p$ , they were calculated using CSMs [10–16]. The analysis delivered parameter-free predictions for both differential and total cross sections from near threshold to very high energies that are in agreement with much available data.

Building further upon Refs. [8, 9], it is relevant to determine whether the reaction mechanism indicated in Fig. 1, with elements calculated using CSMs, can deliver realistic, parameter-free predictions for photoproduction reactions involving other vector mesons, both heavier and lighter than the  $J/\psi$ . The associated comparisons with results from decades of measurements of  $\rho$ ,  $\phi$ ,  $J/\psi$ ,  $\Upsilon$  photoproduction reactions, both differential and total cross sections, over a huge range of energies, would provide valuable information on  $\mathbb{P}$ -exchange universality and other features of photoproduction processes. Notably, spurred by interest in the proton’s gluon content and possible pentaquark states [17–19], the experimental data set has recently been expanded by experiments at Jefferson Lab [20, GlueX] and CERN [21, LHCb].

This discussion is arranged as follows. Section 2 presents the reaction model and our Pomeron exchange

framework for vector meson photoproduction. It is followed, in Sect. 3, by an explanation of the CSM calculation of the Schwinger functions required to obtain the  $\gamma + p \rightarrow V + p$  matrix element sketched in Fig. 1. That matrix element enables completion of the cross section calculations. Section 4 explains how one may infer phenomenological vector-meson–proton scattering lengths from near-threshold differential cross section data using notions of vector meson dominance (VMD). Whilst not rigorous, these scattering lengths can be useful in constraining model studies. They even become objective comparative measures after reinterpretation as a near-threshold slope parameter for each cross section. A large collection of numerical results is reported in Sect. 5 along with relevant data comparisons. That discussion continues in Sect. 6, which analyses the large- $W$  behaviour of photoproduction total cross sections. Numerical results for the near-threshold slope parameter (VMD-based  $V - p$  scattering length) are reported in Sect. 7. Section 8 provides a summary and perspective.

## 2 Reaction model and Pomeron exchange

### 2.1 Dynamical photon to meson transition

The image in Fig. 1 corresponds to the following matrix element [8, 22, 23]:

$$\mathcal{I}_\mu^V(W, t) = \langle V(P; \lambda) p(p_2) | \bar{q} \gamma_\mu q | p(p_1) \rangle = 2 t_{\mu\alpha\nu}^V(q, P) \epsilon_\nu^\lambda(P) \bar{u}(p_2) \tilde{G}_\alpha(w^2, t) u(p_1), \quad (3)$$

where  $\epsilon_\nu^\lambda(P)$  is the  $V$ -meson polarisation vector,  $u(p_1)$ ,  $\bar{u}(p_2)$  are spinors for the incoming and outgoing proton,  $\tilde{G}_\alpha(w^2, t)$  represents the quark-Pomeron-proton interaction; and the factor “2” expresses the equivalence between striking the upper and lower valence quark lines in the quark loop. The invariant mass of the  $\gamma p$  system is  $s = W^2 = -(q + p_1)^2$  and the momentum transfer is  $t = -(p_1 - p_2)^2$ .

The exposed quark loop integration in Fig. 1 receives most support on the neighbourhood  $k^2 \simeq 0$ , *i.e.*, on the domain of near-zero relative momentum within the final state meson, whereat the meson’s Bethe-Salpeter amplitude is peaked. One may therefore write  $w^2 = -(q - P/2 + p_1)^2$ . In this case, the essentially dynamical component of the reaction model, *viz.* the  $\gamma \rightarrow q\bar{q} + \mathbb{P} \rightarrow V$  transition matrix element, can be written as follows:

$$t_{\mu\alpha\nu}^V(q, P) = e_V N_c \text{tr}_D \int \frac{d^4 k}{(2\pi)^4} S_q(k_-) \Gamma_\mu^\gamma(k_-, k_- + q) \times S_q(k_- + q) \Gamma_\alpha^\mathbb{P}(k_- + q, k_+) S_q(k_+) \Gamma_\nu^V(k_+, k_-), \quad (4)$$

where  $N_c = 3$ ;  $e_{\rho^0, \phi, J/\psi, \Upsilon} = e\{1/\sqrt{2}, 1/3, 2/3, 1/3\}$ , the fine-structure constant  $\alpha = e^2/[4\pi]$ ; the trace is

over spinor indices;  $k_{\pm} = k \pm P/2$ ;  $\Gamma_{\nu}^V$  is the Bethe-Salpeter amplitude for an on-shell  $V$  meson – see, *e.g.*, Ref. [24];  $S_q$  is the dressed  $q$  quark propagator; – see, *e.g.*, Ref. [12, Sect. 2.C]; and  $\Gamma_{\mu}^{\gamma}$  is the associated dressed photon-quark vertex. Since we are focusing on photoproduction, then, with complete generality, one may use the Ball-Chiu form for  $\Gamma_{\mu}^{\gamma}$  [25].

The remaining element in Eq. (4) is  $\Gamma_{\alpha}^{\mathbb{P}} = \gamma_{\alpha} \beta_q$ , the Pomeron-quark vertex. Here,  $\beta_q$  is a constant strength factor and  $\gamma_{\alpha}$  is a standard Dirac matrix. We have verified that replacing  $\gamma_{\alpha}$  by some more sophisticated structure, such as the Ball-Chiu vertex [25], for instance, has no material influence: any impact can be absorbed into a modest modification of  $\beta_q$ .

Working in the center of three-momentum frame of the vector-meson–proton system, the relevant four-momenta are:

$$q^{\mu} = (\vec{q}, i|\vec{q}|), \quad (5a)$$

$$P^{\mu} = (\vec{P}, i\sqrt{|\vec{P}|^2 + m_V^2}), \quad (5b)$$

$$p_1^{\mu} = (-\vec{q}, i\sqrt{|\vec{q}|^2 + m_p^2}), \quad (5c)$$

$$p_2^{\mu} = (-\vec{P}, i\sqrt{|\vec{P}|^2 + m_p^2}), \quad (5d)$$

where the metric has uniform positive signature;  $\vec{q}$  is the three-momentum of the on-shell photon;  $\vec{P}$  is the vector-meson three-momentum; and

$$|t|_{\min} = 2|\vec{q}|(|\vec{P}|^2 + m_V^2)^{1/2} - m_V^2 - 2|\vec{q}||\vec{P}|. \quad (6)$$

The differential cross section for exclusive vector meson photoproduction can now be expressed:

$$\frac{d\sigma}{d\Omega} = \frac{1}{4\pi^2} \frac{m_p}{4W} \frac{|\vec{P}|}{k_W} \sum_{\text{proton spin}} (|\mathcal{I}_1|^2 + |\mathcal{I}_2|^2), \quad (7)$$

where

$$k_W = (W^2 - m_p^2)/(2m_p) \quad (8)$$

and  $d\Omega$  is the differential solid-angle element defined by  $\angle \vec{q} \vec{P}$ . The corresponding differential cross section with respect to the momentum transfer is given by

$$\frac{d\sigma}{d(-t)} = \frac{\pi}{|\vec{q}||\vec{P}|} \frac{d\sigma}{d\Omega}. \quad (9)$$

The longitudinal cross section vanishes in photoproduction.

From the expressions sketched above, it is evident that the reaction model, combined with the Pomeron-exchange framework, offers a straightforward approach to studying vector meson photoproduction. The method is computationally economical and has been successfully applied to a broad class of processes; see, *e.g.*, Ref. [26].

## 2.2 Pomeron in the reaction model

The reaction model involves two Pomeron elements. First, the Pomeron-proton content of the coupling is [8, 22, 23]:

$$\tilde{G}_{\alpha}(w^2, t) = \gamma_{\alpha} F_0(t) 3\beta_{\ell} G_{\mathbb{P}}(w^2, t), \quad (10)$$

where “3” enumerates the number of light valence degrees-of-freedom in the proton;  $\beta_{\ell}$  is the strength of the associated Pomeron + light-quark coupling; and  $F_0(t)$  is the empirical nucleon isoscalar elastic electromagnetic form factor. This last factor is well parametrised as follows on the spacelike low- $|t|$  domain relevant herein:

$$F_0(t) = \frac{1 - 2.8t/[4m_p^2]}{1 - t/[4m_p^2]} \frac{1}{(1 - t/t_0)^2}, \quad (11)$$

where  $t_0 = 0.71 \text{ GeV}^2$ .

The second element in Eq. (10) is typically called the Pomeron propagator:

$$G_{\mathbb{P}}(s, t) = \left[ \frac{s}{s_0} \right]^{\alpha_{\mathbb{P}}(t)-1} \exp \left[ -i \frac{\pi}{2} (\alpha_{\mathbb{P}}(t) - 1) \right], \quad (12)$$

with  $\alpha_{\mathbb{P}}(t) = \alpha_0 + \alpha_1 t$ ,  $s_0 = 1/\alpha_1$ , and  $\alpha_{0,1}$  fitted to selected small- $|t|$ , large- $W$  meson photoproduction data within the context of Regge phenomenology:  $\alpha_0$  is fixed by the energy dependence of the total cross section and  $\alpha_1$  by the  $t$ -slope of the differential cross section – see, *e.g.*, Refs. [27, 28]. These parameters depend on whether the final-state vector meson is light or heavy [29].

## 2.3 VMD-like treatment of photon to meson transition

In the following, we will compare our predictions with those obtained using a simplified framework that replaces the calculated  $\gamma \rightarrow \bar{q}q + \mathbb{P} \rightarrow V$  transition matrix element by a phenomenologically constrained model. Sketched in Fig. 2 and identified as the  $\mathbb{P}$ –am model in Ref. [9], this approach is obtained by beginning with the Ref. [34] model; setting  $v_{cN} = 0$ , so the quark-loop integration, based on a constituent quark model wavefunction, and  $V - N$  final state interactions (FSIs) do not contribute to the amplitude; and updating the Pomeron trajectories and Pomeron-quark couplings.

The associated matrix element for diffractive vector meson photoproduction is

$$\begin{aligned} \mathcal{I}_{\mu}(W, t) \propto & \bar{u}(p_2) \gamma_{\alpha} u(p_1) \epsilon_{\nu}^{\lambda}(P) \Gamma_{\alpha, \mu\nu} G_{\mathbb{P}}(w^2, t) \\ & \times [\beta_q F_V(t)][\beta_l F_0(t)], \end{aligned} \quad (13)$$

with the tensor structure of the  $\mathbb{P}$ – $V$  vertex being [35]

$$\Gamma_{\alpha, \mu\nu} = q_{\alpha} \delta_{\mu\nu} - q_{\mu} \delta_{\alpha\nu}. \quad (14)$$

Table 1: Quark current-masses and parameters characterising the CSM interaction kernels for the mesons considered herein. The quark current masses are quoted at a renormalisation scale  $\zeta = \zeta_{19} = 19$  GeV, *i.e.*, in the far ultraviolet so as to avoid truncation ambiguity. The  $u, d$  values were chosen to reproduce  $m_\pi, f_\pi$ ; the kaon mass was used to fix  $m_s$ ;  $m_c$  was chosen to yield the  $\eta_c$  mass; and the  $\eta_b$  mass was used to fix  $m_b$  [30]. Using one-loop evolution, the listed light quark masses correspond to  $\zeta = \zeta_2 = 2$  GeV values of  $m_\ell^{\zeta_2} = 0.0048$  GeV,  $m_s^{\zeta_2} = 0.117$  GeV; and regarding the heavy quarks, the listed values equate to the following Euclidean constituent quark masses [31],  $M_c = 1.41$  GeV,  $M_b = 4.34$  GeV. All four masses correspond to those typically quoted in connection with the given flavour and are a fair match with contemporary inferences [32]. The same Pomeron trajectory is used for both  $\rho^0$  and  $\phi$  photoproduction [8], and another for  $J/\psi$  and  $\Upsilon$  [33, ZEUS]. Pomeron-quark couplings,  $\beta_q$ , for both reaction models considered herein – Sects. 2.1, 2.3 – are determined as described in Sect. 2.4.

Meson	Gluon model					P trajectory		P-dyn	P-am
	$m_{\zeta_{19}}$ [GeV]	$D\omega$ [GeV $^3$ ]	$\omega$ [GeV]	$N_f$	$\Lambda_{\text{QCD}}$ [GeV]	$\alpha_0$	$\alpha_1$ [GeV $^{-2}$ ]	$\beta_q$ [GeV $^{-1}$ ]	$\beta_q$ [GeV $^{-1}$ ]
$\rho_\ell^0$	0.0034	0.8 $^3$	0.5	4	0.234	1.1	0.33	3.5	1.96
$\phi_s$	0.083	0.8 $^3$	0.5	4	0.234	1.1	0.33	1.89	1.51
$J/\psi_c$	0.89	0.6 $^3$	0.8	4	0.234	1.2	0.115	0.11	0.428
$\Upsilon_b$	3.59	0.6 $^3$	0.8	5	0.36	1.2	0.115	0.016	0.638

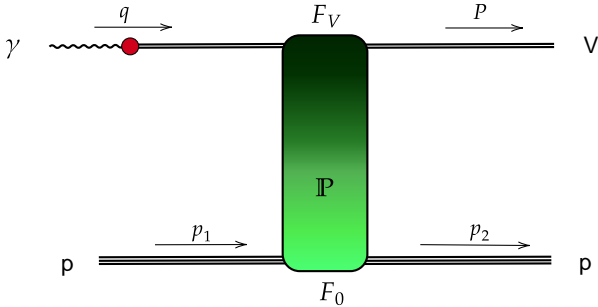


Fig. 2: P-am reaction model for  $\gamma + p \rightarrow V + p$ . Compared with our dynamical model, P-dyn, sketched in Fig. 1, P-am replaces the  $\gamma \rightarrow q\bar{q} + \mathbb{P} \rightarrow V$  transition matrix element by a momentum-independent  $\gamma \rightarrow V$  transition coupling (akin to vector meson dominance) along with a form factor,  $F_V$ , that expresses a Pomeron–vector-meson form factor.

The constants  $\beta_{q,\ell}$  fix the strengths of P interactions with the quarks in the vector mesons and the proton, respectively. Drawn from Ref. [34], the phenomenological form factor

$$F_V(t) = \frac{1}{m_V^2 - t} \left( \frac{2\mu_0^2}{2\mu_0^2 + m_V^2 - t} \right), \quad (15)$$

$\mu_0 = 1.1$  GeV, replaces the momentum dependence of the  $\gamma \rightarrow q\bar{q} + \mathbb{P} \rightarrow V$  loop and vastly simplifies its tensor structure.

#### 2.4 Pomeron trajectories and couplings

In the subsequent calculations, we adopt Pomeron trajectories that are either well-established or reliably in-

ferred, enabling accurate descriptions of existing experimental data [8, 33, 36]. A common trajectory is used for light mesons and another for the heavy systems; see Table 1. The coupling  $\beta_u$  is determined via a least-squares fit to the differential cross section for  $\rho^0$  photoproduction [37, ZEUS1995]. (The  $\beta_u$  value used herein is 25% larger than that in Ref. [9] as a consequence of correcting a coding error in that analysis.) The couplings  $\beta_s$  and  $\beta_b$  are obtained through fits to high-energy total cross-section data on  $\phi$  [38] and  $\Upsilon$  production [39–43]; and the  $\beta_c$  values are fixed, as in Ref. [9], by requiring a best fit to the  $W$ -dependence of the  $|t| \approx |t|_{\min} J/\psi$  photoproduction differential cross section in Ref. [33, ZEUS 2002].

### 3 Photon to vector meson transition amplitude in CSMs

The photoproduction reaction mechanism sketched in Fig. 1 involves the dressed quark propagator, dressed photon-quark vertex; and vector-meson Bethe-Salpeter amplitude. Such quantities have long been the focus of CSM studies and many relevant reviews are available; see, *e.g.*, Refs. [10–16, 44–46]. Hence, today, these quantities are readily computed, so it is possible to arrive at parameter-free predictions for the  $\gamma \rightarrow q\bar{q} + \mathbb{P} \rightarrow V$  transition matrix elements,  $t_{\mu\nu\lambda}(q, P)$  in Eq. (4). The key to such calculations is the quark+antiquark scattering kernel. For this, the leading-order (rainbow-ladder, RL) truncation [47, 48] is obtained by writing [49]:

$$\mathcal{K}_{tu}^{rs}(k) = \tilde{\mathcal{G}}(y)[i\gamma_\mu \frac{\lambda^a}{2}]_{ts}[i\gamma_\nu \frac{\lambda^a}{2}]_{ru} T_{\mu\nu}(k), \quad (16)$$

Table 2: Pion and vector meson masses and leptonic decay constants computed herein, using CSMs, compared with experimental values [32, PDG], quoted at a sensible level of precision. Regarding vector mesons, the mean absolute relative difference between prediction and experiment is 5(3)%.

Meson	Mass [GeV]		Decay constant [GeV]	
	Herein	Expt.	Herein	Expt.
$\pi$	0.138	0.138	0.092	0.092
$\rho^0$	0.741	0.775	0.149	0.153
$\phi$	1.086	1.019	0.183	0.168
$J/\psi$	3.123	3.097	0.278	0.294
$\Upsilon(1s)$	9.52	9.46	0.558	0.51

$k^2 T_{\mu\nu}(k) = k^2 \delta_{\mu\nu} - k_\mu k_\nu$ ,  $y = k^2$ . The tensor structure corresponds to Landau gauge, used because it is both a fixed point of the renormalisation group and that gauge for which corrections to RL truncation are least noticeable [50]. In Eq. (3),  $r, s, t, u$  represent colour, spinor, flavour matrix indices (as necessary).

A realistic form of  $\tilde{G}(y)$  is explained in Refs. [51, 52]:

$$\tilde{G}(y) = \frac{8\pi^2}{\omega^4} D e^{-y/\omega^2} + \frac{8\pi^2 \gamma_m \mathcal{F}(y)}{\ln [\tau + (1 + y/\Lambda_{\text{QCD}}^2)^2]}, \quad (17)$$

$\mathcal{F}(y) = \{1 - \exp(-y/\Lambda_I^2)\}/y$ ,  $\Lambda_I = 1 \text{ GeV}$ ;  $\tau = e^2 - 1$ ;  $\gamma_m = 12/(33 - 2N_f)$ , with  $N_f$  and  $\Lambda_{\text{QCD}}^{N_f}$  given in Table 1. In solving all relevant Schwinger function equations, we use a mass-independent (chiral-limit) momentum-subtraction renormalisation scheme [53], with renormalisation scale  $\zeta = 19 \text{ GeV}$ . At this scale, the quark wave function renormalisation constants are practically unity.

Applications to numerous systems and reactions have established [14] that interactions in the class typified by Eqs. (3), (17) can unify the properties of many systems. Notably, when  $\omega D =: \zeta^3$  is held fixed, results for observable quantities remain practically unchanged under  $\omega \rightarrow (1 \pm 0.2)\omega$  [54]. Thus, the interaction in Eq. (17) is determined by just one parameter:  $\zeta^3 := \omega D$ .

In the light-quark sector,  $f = u, d, s$ ,  $\zeta_f = 0.8 \text{ GeV}$  delivers a good description of a range of pseudoscalar and vector meson static properties; see Table 2 and Fig. 3. These results were obtained as explained, *e.g.*, in Refs. [55–57]. As noted above, the procedure involves solving sets of coupled gap and Bethe-Salpeter equations.

For heavier quarks, it is known that corrections to RL truncation are less important – see, *e.g.*, Ref. [58] for illustration, so the interaction parameter should be closer to that used in more sophisticated kernels. This

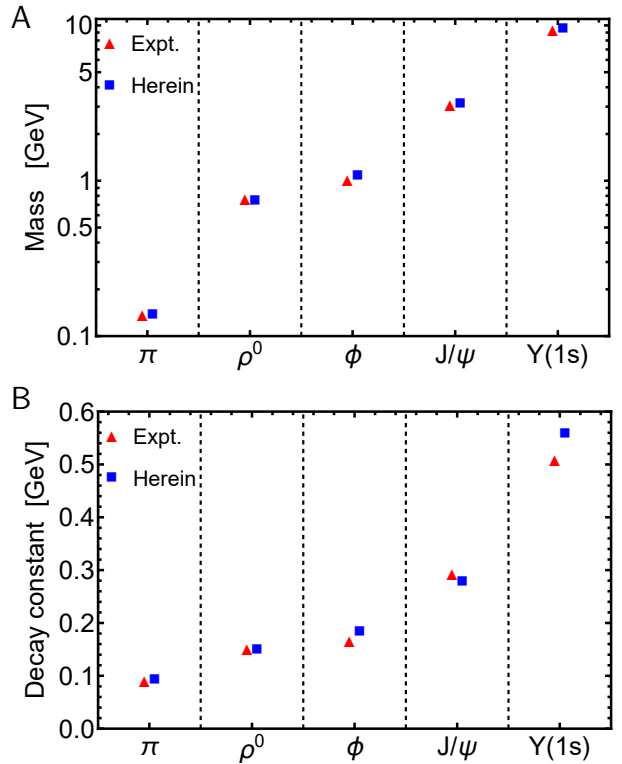


Fig. 3: Pion and vector meson properties listed in Table 2, computed using CSMs with interaction parameters in Table 1 [30, 57, 59]: (A) Masses and (B) leptonic decay constants. Blue squares indicate CSM results; red triangles indicate experimental values at a sensible level of precision [32].

is discussed further in, *e.g.*, Ref. [57, Sect. IIB], and explains the  $c, b$  quark values listed in Table 1, which deliver the results listed in Table 2 and drawn in Fig. 3.

#### 4 Near-threshold slope parameter / meson-proton scattering lengths

Diffractive exclusive vector meson photoproduction near threshold provides insights into the low-energy meson-proton interaction, which is often characterised by a scattering length. Despite its failings [24], especially in applications to heavier vector mesons, many phenomenological studies continue to use vector meson dominance as a phenomenological tool. Within that framework, the photoproduction cross section  $\sigma_{\gamma p \rightarrow Vp}$  is simply related to the meson-proton elastic scattering cross section,  $\sigma_{Vp \rightarrow Vp}$ , such that, near threshold, the differential cross section can be expressed as follows [60]:

$$\left. \frac{d\sigma^{\gamma p \rightarrow Vp}}{d\Omega} \right|_{\text{th}} = \frac{|\vec{P}|}{|\vec{q}|} \frac{1}{64\pi} |T^{\gamma p \rightarrow Vp}|^2,$$

$$\begin{aligned}
&= \frac{|\vec{P}|}{|\vec{q}|} \frac{\pi\alpha}{g_V^2} \frac{d\sigma^{Vp \rightarrow Vp}}{d\Omega} \Big|_{\text{th}} \\
&= \frac{|\vec{P}|}{|\vec{q}|} \frac{\pi\alpha}{g_V^2} |\alpha_{Vp}|^2,
\end{aligned} \tag{18}$$

where  $\alpha$  is the fine-structure constant,  $\vec{q}$  and  $\vec{P}$  are the initial and final momenta of the photon and vector meson, respectively – Eq.(5), and  $\alpha_{Vp}$  is the model meson-proton scattering length. The VMD ingredient is the coupling  $g_V$ , which is defined by the vector meson's electromagnetic decay width  $\Gamma_{V \rightarrow e^+e^-}$ :

$$g_V^2 = \frac{\pi\alpha^2 m_V}{3\Gamma_{V \rightarrow e^+e^-}}. \tag{19}$$

Our prediction for this differential cross section is given in Eq. (7). That is the formula we use to evaluate all results. However, by equating our predictions with Eq. (18) one can arrive at model-specific VMD values for the meson-proton scattering length. These can be used as single parameters with which to evaluate the veracity of existing such model dependent inferences of meson-proton scattering lengths [60–63]. Furthermore, obtained in this way, one need not interpret  $|\alpha_{Vp}|$  as the  $V - p$  scattering length. Instead, it can be viewed as a near-threshold slope parameter. Then, the value has objective utility as a comparison between theory and experiment.

## 5 Results: cross sections

With the quark current-masses and interaction parameters, Table 1 – and the propagators and Bethe-Salpeter amplitudes they produce – validated in comparisons with experimental values for meson masses and decay constants, Table 2 and Fig. 3, we use these elements to calculate the matrix elements defined by Eqs. (3), (4).

Accounting for current-conservation and the fact that  $P_\nu \Gamma_\nu^V = 0$ , then, in all cases,  $t_{\mu\nu\alpha}^V$  involves 9 independent scalar functions which modulate the strength of the allowed tensor structures:

$$t_{\mu\nu\alpha}^V(q, P) = \sum_{i=1}^9 F_i^V(q, P) \tau_{\mu\nu\alpha}^i(q, P). \tag{20}$$

The nine tensors are listed explicitly in Appendix A.

Each scalar function in Eq. (20) is readily extracted using sensibly chosen projection operators. In practice, we find that the scalar function associated with the tensor structure

$$\tau_{\mu\nu\alpha}^1(q, P) = q_\alpha (\delta_{\mu\nu} - P_\mu P_\nu / P^2) \tag{21}$$

gives the dominant contribution to the photoproduction cross sections in all cases: for heavy mesons,  $J/\psi, \Upsilon$ , all

other tensors can be neglected; and for light mesons,  $\rho, \phi$ , it provides roughly 85% of the cross section, with the tensor

$$\tau_{\mu\nu\alpha}^2(q, P) = P_\alpha (\delta_{\mu\nu} - P_\mu P_\nu / P^2) \tag{22}$$

contributing the remaining 15% – alone (5%) and via constructive interference with  $\tau^1$  (10%). Notwithstanding these observations, all tensor structures are employed to produce the results reported herein.

For each vector meson, we calculate both the differential and total cross sections for exclusive photoproduction. The differential cross section depends on  $W$ , the centre-of-mass energy, and  $t$ , the square-momentum transfer. When relevant data are available, we examine both the  $W$ - and  $t$ -dependence. Often, the  $W$  dependence is analysed at  $|t| = |t|_{\min}$ , Eq. (6), which corresponds to forward scattering, *i.e.*, the smallest possible value for which the vector meson can be produced leaving the proton in tact. The cross sections are largest on this domain and very sensitive to reaction details. For instance, within our approach, they are much affected by the quark-loop dynamics expressed by Fig. 1, as shown for the  $J/\psi$  in Ref. [9] and we will see again herein for other vector mesons. On the other hand, the  $t$ -dependence of the differential cross sections are usually mapped at fixed  $W$ . Near threshold, they, too, are sensitive to the vector meson production mechanism.

It is worth noting here that in fixed-target experiments, the photon energy is often used as the primary variable, *viz.*  $E_\gamma(W) = k_W$  in Eq. (8).

### 5.1 $\rho$ photoproduction

Calculated using the Pomeron trajectory and quark–Pomeron couplings given in Table 1 – Row 1, our predictions for  $\gamma + p \rightarrow \rho^0 + p$  photoproduction are presented in Figs. 4 and 5.

In Fig. 4, we draw the total cross section on  $W \in [W_{\text{th}}^\rho, 500 \text{ GeV}]$  along with data from a variety of sources [64, AHM], [65, BCEGLMOPRS], [66, 67, SLAC], [68, FNAL], [69, 70, H1], plus pseudodata obtained from differential  $\pi^+ \pi^- p$  photoproduction cross sections measured with the CLAS detector at JLab, analysed within the JLab–Moscow State University (JM) model [71], and integrated over the differential solid angle. Both  $\mathbb{P}-\text{dyn}$  and  $\mathbb{P}-\text{am}$  reproduce the data on  $W \gtrsim 10 \text{ GeV}$ , which may therefore be identified as the domain of Pomeron dominance in this case. Furthermore, the  $\mathbb{P}-\text{dyn}$  model is satisfactory on  $W \gtrsim 5 \text{ GeV}$ , highlighting the importance of a sound description of the quark loop in Fig. 1. However, both models are equally poor on  $W \in [W_{\text{th}}^\rho, 5 \text{ GeV}]$ . This is because the proton and  $\rho$

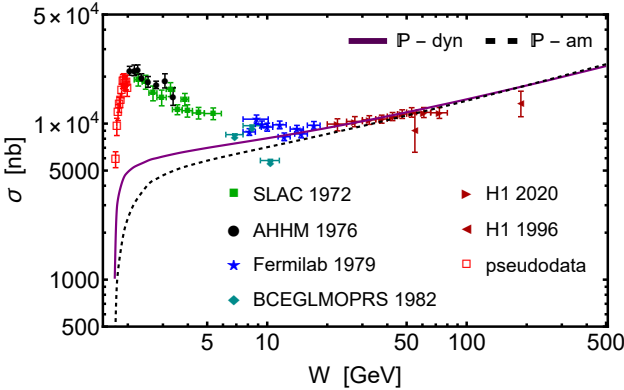


Fig. 4:  $W$ -dependence of total cross section for  $\rho^0$  photoproduction,  $W_{\text{th}}^\rho = 1.714$  GeV. Solid purple curve –  $\mathbb{P}$ –dyn; dashed black curve –  $\mathbb{P}$ –am. Data sources: black circles – [64, AHHM]; cyan diamonds (fixed target) – [65, BCEGLMOPRS]; green squares [66, 67, SLAC]; blue stars [68, FNAL]; red left and right triangles [69, 70, H1]; and red open squares – pseudodata inferred [63] from differential  $\pi^+\pi^-p$  photoproduction cross sections measured with CLAS at JLab and analysed within the JM model [71] (see text).

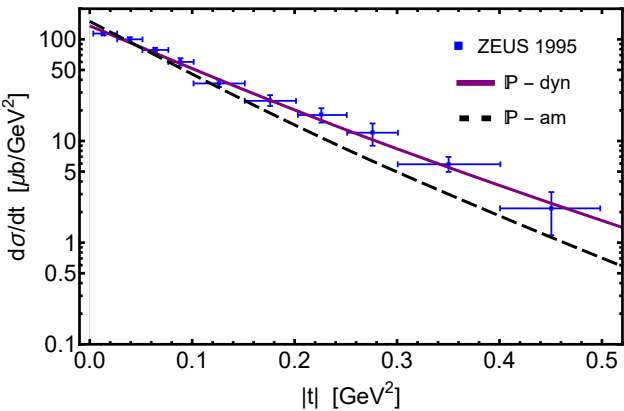


Fig. 5: Differential cross section for  $\rho^0$  photoproduction compared with data [37, ZEUS] (blue squares) in the range  $60 < W < 80$  GeV. Solid purple curve –  $\mathbb{P}$ –dyn; dashed black curve:  $\mathbb{P}$ –am. Both are computed at the average energy  $W = 70$  GeV. Pomeron trajectory and quark–Pomeron couplings used are given in Table 1 – Row 1.

meson share valence quarks; hence, many additional (nondiffractive) exchange contributions are possible in the photoproduction reaction. For instance, a leading-order calculation using a phenomenological meson-exchange model [72] is able to reproduce the low- $W$  data [8, Fig. 15]. Such contributions decay rapidly with  $W$ , so that the diffractive  $\mathbb{P}$ –dyn reaction model becomes valid on  $W \gtrsim 5$  GeV.

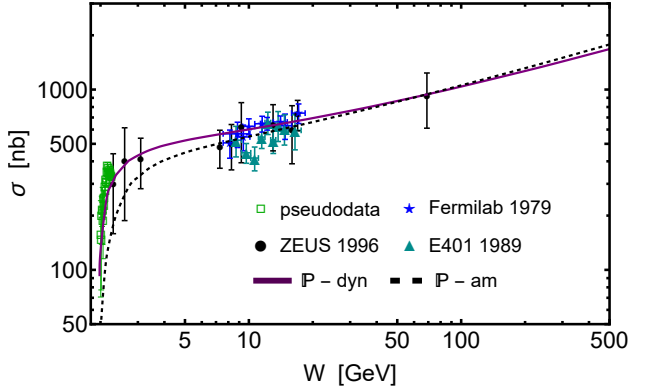


Fig. 6:  $W$ -dependence of total cross section for  $\phi$  photoproduction,  $W_{\text{th}}^\phi = 1.958$  GeV. Solid purple curve –  $\mathbb{P}$ –dyn; dashed black curve –  $\mathbb{P}$ –am. Data: blue stars – [68, FNAL]; cyan triangles – [74, E401]; black circles – [38, ZEUS]; and green open squares “pseudodata” [61], obtained by interpolating CLAS differential cross sections [75, CLAS] as described in the text.

Figure 5 depicts the differential cross section. It compares  $\mathbb{P}$ –dyn and  $\mathbb{P}$ –am predictions with data from Ref. [37, ZEUS] in the range  $60 < W < 80$  GeV. Our results are evaluated at the average experimental energy,  $W = 70$  GeV. Recalling that the Pomeron trajectory parameters in Table 1 – Row 1 were taken from Ref. [8] and only the quark–Pomeron couplings were tuned to the data in Fig. 4 – see Sec. 2.4 – then it becomes clear that the quark-loop dynamics in Fig. 1 has an impact on the differential cross section even far above threshold,  $W \gg W_{\text{th}}^\rho$ .

Regarding  $\omega$ -meson photoproduction, owing to its comparable structure, similar features and explanations pertain to the cross sections [73].

## 5.2 $\phi$ photoproduction

Using the Pomeron trajectory and quark–Pomeron couplings given in Table 1 – Row 2, we obtain the predictions for  $\gamma + p \rightarrow \phi + p$  photoproduction cross sections presented in Figs. 6–10. An important difference between this reaction and  $\rho^0$  photoproduction is that the  $\phi$ -meson contains no valence quarks in common with the proton; hence, fewer nondiffractive processes are possible.

The total cross section,  $\sigma_{\gamma p \rightarrow \phi p}$ , is drawn in Fig. 6. Comparing the  $\mathbb{P}$ –dyn and  $\mathbb{P}$ –am predictions with data, it is evident that the dynamical quark loop associated with Fig. 1 is crucial in order to obtain agreement with data. This is especially true near threshold. Notably, very near threshold, direct measurements of  $\sigma_{\gamma p \rightarrow \phi p}$  are unavailable. To fill that gap, Ref. [61] generated

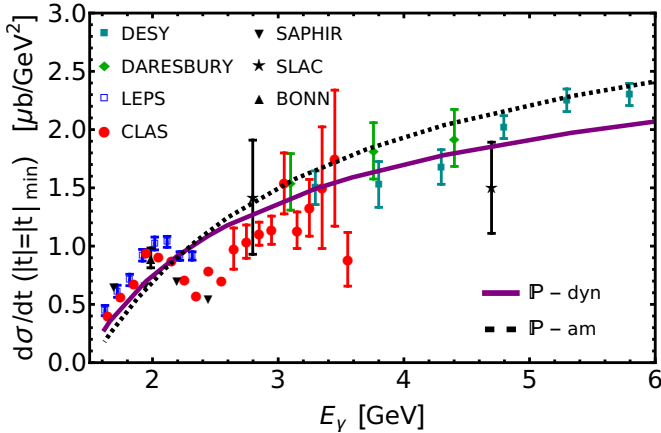


Fig. 7:  $E_\gamma$  dependence of differential cross section for  $\phi$  photoproduction, evaluated at  $|t| = |t|_{\min}$ , Eq. (6), corresponding to forward-angle scattering. Solid purple curve –  $\mathbb{P}$ –dyn; dashed black curve –  $\mathbb{P}$ –am. Data: black stars – [76, SLAC]; black up triangles – [77, Bonn]; cyan squares – [78, DESY]; green – [79, Daresbury]; black down triangles – [80, SAPHIR]; blue open squares – [81, LEPS]; red circles – [82, CLAS].

pseudodata by interpolating differential cross sections measured at JLab [75, CLAS] and integrating over the differential solid angle. The  $\mathbb{P}$ –dyn prediction aligns well with this pseudodata, too; although it misses the “bump” apparent in the pseudodata. We note that this bump may be merely an artefact of the pseudodata construction procedure.

The  $E_\gamma$  dependence of the forward-angle  $\phi$  photoproduction differential cross section is drawn in Fig. 7. Compared with data, the  $\mathbb{P}$ –dyn reaction model delivers a better global description than  $\mathbb{P}$ –am; hence, our dynamical treatment of the  $\gamma \rightarrow q\bar{q} + \mathbb{P} \rightarrow \phi$  transition is once more seen to be important.

The  $|t|$  dependence of the  $\phi$  photoproduction differential cross section is depicted in Fig. 8 for two different but low photon energies. On  $|t| \lesssim 2 \text{ GeV}^2$ , the  $\mathbb{P}$ –dyn reaction model provides a good description of the data [75, CLAS 13], [79, Daresbury], [83, CLAS 00]. However, the reaction is not purely diffractive on  $|t| \gtrsim 2 \text{ GeV}^2$ : on this domain, one sees structure, likely associated with baryon resonance excitation. The mismatch between  $\mathbb{P}$ –am and data on the entire domain depicted highlights the importance of a realistic description of the  $\gamma \rightarrow q\bar{q} + \mathbb{P} \rightarrow V$  transition, Fig. 1.

Figures 9, 10 compare  $\mathbb{P}$ –dyn predictions for the  $|t|$ -dependence of the  $\phi$  photoproduction differential cross sections with data available at lower photon energies than those in Fig. 8, *viz.* Refs. [75, CLAS 13], [80, SAPHIR], [81, LEPS]. Regarding Fig. 9, in this case, too, the agreement between our reaction model and data for

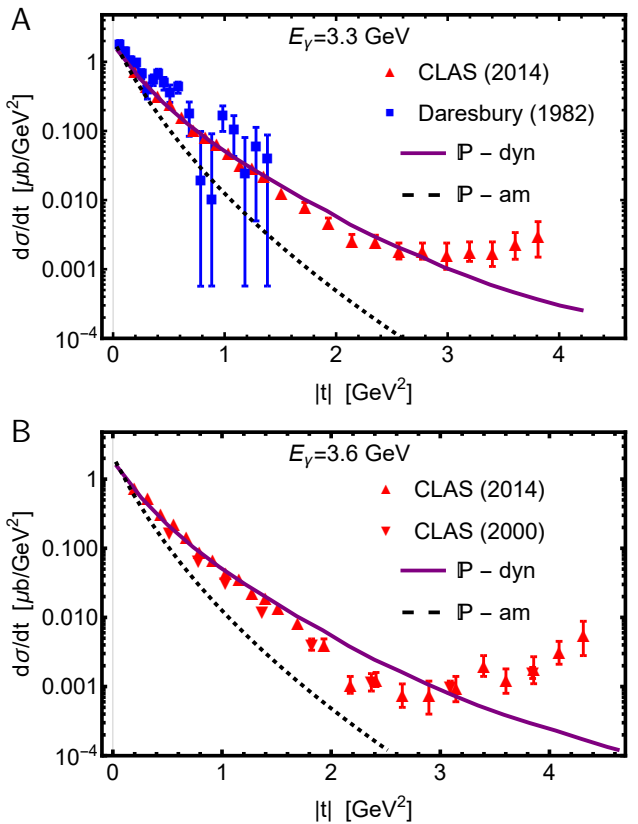


Fig. 8:  $|t|$  dependence of differential cross section for  $\phi$  photoproduction at photon energies:  $E_\gamma = 3.3 \text{ GeV}$  ( $W \approx 2.66 \text{ GeV}$ ) and  $E_\gamma = 3.6 \text{ GeV}$  ( $W \approx 2.76 \text{ GeV}$ ). Solid purple curve –  $\mathbb{P}$ –dyn; dashed black curve –  $\mathbb{P}$ –am. Data: red up-triangles – [75, CLAS 2014]; blue squares – [79, Daresbury] (Panel A); red down-triangles – [83, CLAS 2000] (Panel B).

near-forward scattering is good. The mismatch at larger  $|t|$  was already discussed in connection with Fig. 8. Concerning Fig. 10, the  $\mathbb{P}$ –dyn provides a good description of the differential cross section except, perhaps, in the neighbourhood  $E_\gamma \simeq 2 \text{ GeV}$ , whereupon some non-diffractive processes may be contributing somewhat to the production process.

### 5.3 $J/\psi$ photoproduction

The reaction model characterised by the sketch in Fig. 1,  $\mathbb{P}$ –dyn, was applied to  $J/\psi$  photoproduction in Ref. [9]. Herein, for completeness, we recapitulate and somewhat extend the results described in that study. Of course, the  $J/\psi$  contains no valence degrees of freedom in common with the proton; so, it has long been widely held [29, 84] that the dominant mechanisms underlying  $J/\psi$  photoproduction must involve some manifestations of gluon physics within the target proton and, perhaps,

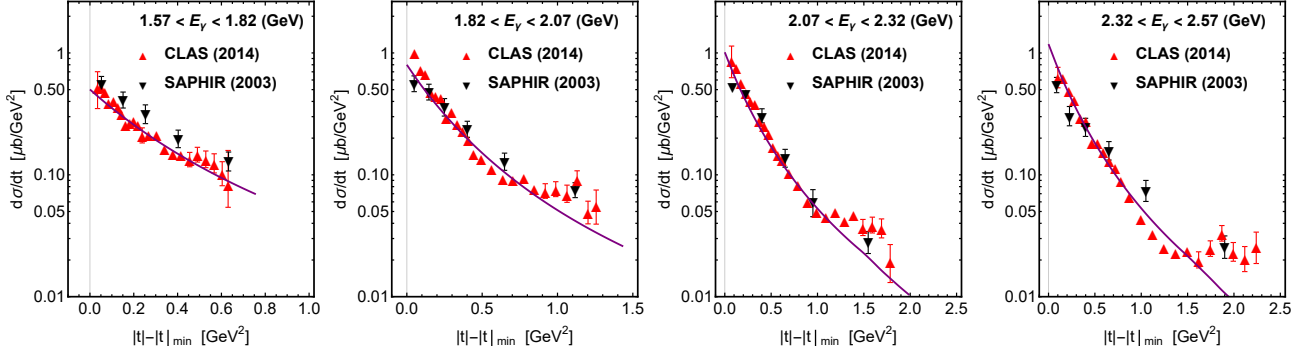


Fig. 9: Differential cross sections for  $\phi$  photoproduction as a function of  $|t| - |t|_{\min}$ , Eq. (6), at low photon energies,  $E_\gamma$ . Solid purple curve –  $\mathbb{P}$ -dyn. Data: red up-triangles – [75, CLAS 2014]; black down-triangles – [80, SAPHIR].

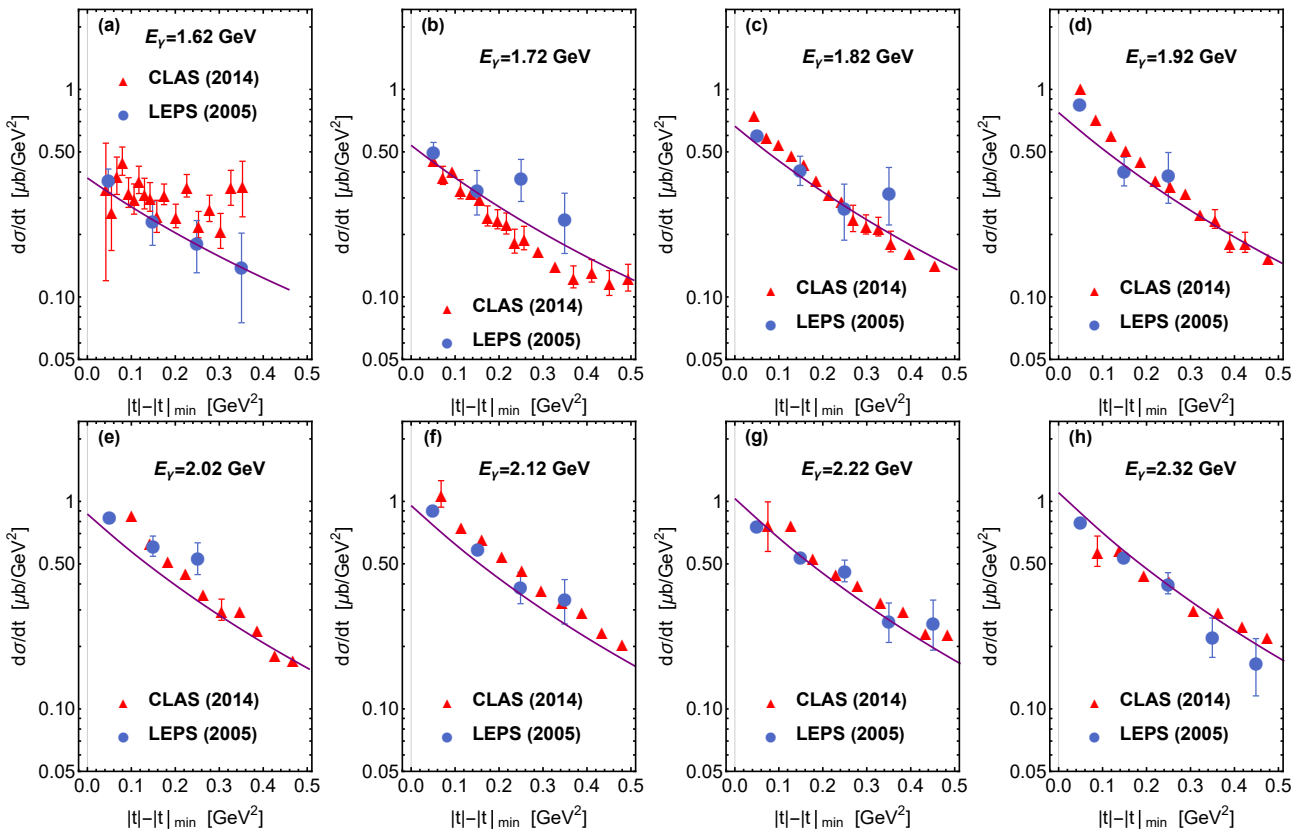


Fig. 10: Differential cross sections for  $\phi$  photoproduction as a function of  $|t| - |t|_{\min}$  at low photon energies,  $E_\gamma$ . Solid purple curve –  $\mathbb{P}$ -dyn. Data: red up-triangles – [75, CLAS 2014]; blue circles – [81, LEPS].

the incipient vector meson, and/or the exchange of (perhaps infinitely many, correlated) gluons between the partonic constituents of each. (This latter is a Pomeron-like effect.)

The  $J/\psi$  process is topical because some have argued [85] that there is a connection between near-threshold  $J/\psi$  photoproduction and the in-proton expectation value of the QCD trace anomaly; hence, insights into the character of emergent hadron mass (EHM) [12–16, 86–89]. This possibility has served as a motivation

for new high-energy, high-luminosity accelerator facilities [17–19]. However, any trace-anomaly connection now appears remote [24, 34, 90, 91]. Notwithstanding these remarks, there is a continuing desire to interpret  $\gamma + p \rightarrow V + p$  photoproduction data in terms of gluon physics; hence, an elucidation of the underlying reaction mechanism is crucial.

As discussed in Sect. 2.4 and in Ref. [9], the Pomeron- $c$ -quark coupling was fixed by requiring a best least-squares fit to the  $W$ -dependence of the  $|t| \approx |t|_{\min}$   $J/\psi$

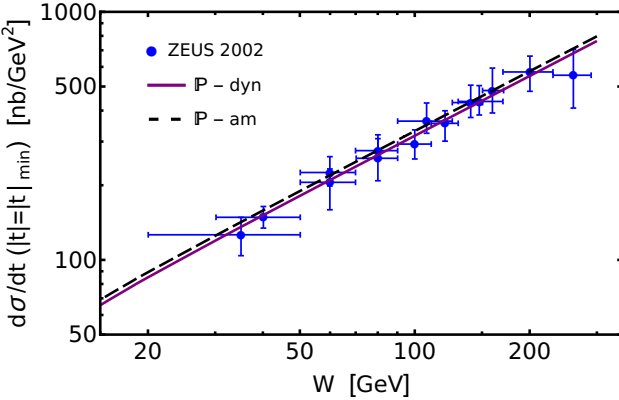


Fig. 11: Differential cross-section for  $\gamma p \rightarrow J/\psi p$  on  $|t|/m_p \simeq 0$  (forward). Solid purple curve:  $\mathbb{P}$ -dyn; dashed black curve -  $\mathbb{P}$ -am. (Pomeron parameters in Table 1 – Row 3.) Data from Ref. [33, ZEUS 2002].

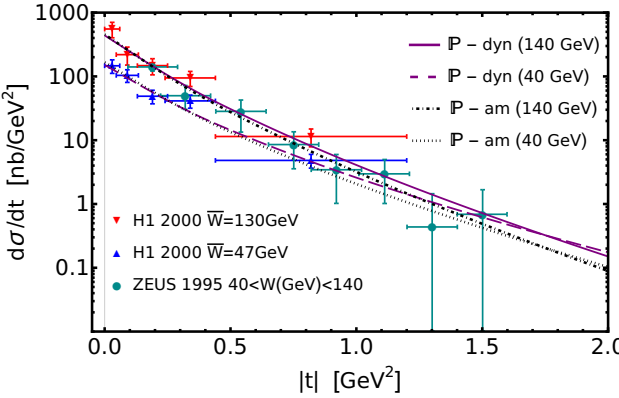


Fig. 12: Predicted  $|t|$  dependence of differential cross section for  $J/\psi$  photoproduction at selected  $W$  values well above threshold. Solid purple curve –  $\mathbb{P}$ -dyn,  $W = 140$  GeV; dashed purple curve –  $\mathbb{P}$ -dyn,  $W = 40$  GeV; dot-dashed black curve –  $\mathbb{P}$ - am,  $W = 140$  GeV; dotted black curve –  $\mathbb{P}$ - am,  $W = 40$  GeV. Data, with  $\bar{W}$  being experimental mean  $W$ : blue up-triangles – [40, H1 2000]; red down-triangles – [40, H1 2000]; cyan circles – [92, ZEUS 1995].

photoproduction differential cross section in Ref. [33, ZEUS 2002]. The results are displayed in Fig. 11. From this point, all  $J/\psi$  results are predictions of our reaction model. Thus, it is significant that, as illustrated in Fig. 12, our reaction model provides a good description of the  $(W, t)$  dependence of the differential cross sections reported in Ref. [40, H1 2000]. Evidently, with increasing  $|t|$  high- $W$  data retain some sensitivity to the dynamical quark loop in Fig. 1: compare  $\mathbb{P}$ -dyn with  $\mathbb{P}$ -am on  $|t| \gtrsim 1$  GeV $^2$ .

Figure 13 depicts our predictions for the  $\gamma p \rightarrow J/\psi p$  differential cross section as a function of  $|t|$  at energies

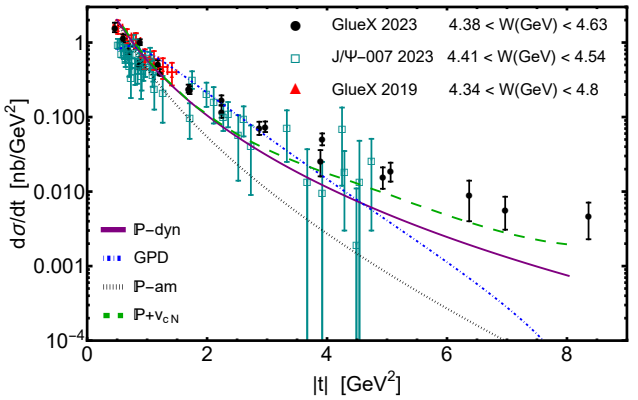


Fig. 13: Differential cross-section for  $\gamma p \rightarrow J/\psi p$ . Solid purple curve –  $\mathbb{P}$ -dyn; dotted purple curve –  $\mathbb{P}$ -am; dot-dashed blue curve – GPD model [93]; dashed green curve – Pomeron +  $J/\psi N$  scattering model [34]. (Predictions herein obtained with Pomeron parameters in Table 1 – Row 3.) Data:  $4.43 < W/\text{GeV} < 4.8$  – [94, GlueX 2019];  $4.38 < W/\text{GeV} < 4.63$  – [20, GlueX 2023];  $4.41 < W/\text{GeV} < 4.54$  – [95,  $J/\psi$ -007]. (All theory curves computed using  $W = 4.5$  GeV.)

not too far above threshold,  $W_{\text{th}}^{J/\psi} = 4.04$  GeV. Evidently, on this  $W$  domain, the momentum-dependence of the  $\gamma \rightarrow c\bar{c} + \mathbb{P} \rightarrow J/\psi$  transition loop in Fig. 1 has a significant influence. Again, this is highlighted by the difference between the  $\mathbb{P}$ -dyn and  $\mathbb{P}$ -am predictions.

Along with our parameter-free predictions, we also draw the result obtained using a GPD model [93], which involves three parameters and assumes specific, simple forms for the two gluon gravitational form factors: the parameters were fixed via a least-squares fit to the data in Refs. [20, 95]. Citing Ref. [9], quantitatively, the GPD model's description of  $J/\psi$ -007 data [95] is better than its match with the GlueX points [20]. In this outcome, there is a signal of overfitting, the probability of which is increased by the result for  $d\sigma/dt$  being a concave function on the entire plotted  $|t|$  domain, with a global maximum on  $|t| \simeq 0.7$  GeV $^2$ . This is qualitatively inconsistent with the other reaction models, which deliver a differential cross-section that is a monotonically decreasing convex function.

The remaining curve in Fig. 13 is the result from Ref. [34], which argues that  $J/\psi$  photoproduction should be described by Pomeron exchange augmented by a  $c$ -quark+nucleon potential,  $v_{cN}$ , that drives  $J/\psi N$  scattering and FSIs, with the FSIs dominating near threshold. This result is similar to our favoured  $\mathbb{P}$ -dyn prediction on  $|t| \lesssim 2.5$  GeV $^2$  and thereafter becomes harder. Again citing Ref. [9], quantitatively, the FSIs in the  $\mathbb{P} + v_{cN}$  reaction model improve the description of GlueX data but degrade that of  $J/\psi$ -007. Looking harder, one

finds that the most reasonable description of available near-threshold  $d\sigma/dt$  data is provided by our  $\mathbb{P}$ -dyn reaction model: this parameter-free prediction delivers a monotonically decreasing convex differential cross-section and a  $\chi^2/\text{degree-of-freedom}$  that does not vary excessively across the data sets [9].

These observations show that whilst modern Poincaré covariant calculations do indicate that the proton mass radius,  $r_m$ , is smaller than its charge radius [96], owing to the different character of the effective probe [97], one is not justified in drawing any link between the Ref. [95,  $J/\psi$ -007] data and a measurement of  $r_m$  or, indeed, any other quantity inferred via a GPD-specific interpretation of those or other data.

We take a closer look at near-threshold  $J/\psi$  photoproduction in Fig. 14 by exploring the  $(E_\gamma, |t|)$  dependence of the differential cross-section. Very close to threshold, Fig. 14 A, the Ref. [20, GlueX] data suggest a role for some nondiffractive contributions to the reaction on  $|t| \gtrsim 3 \text{ GeV}^2$ . This domain is not reached by the Ref. [95,  $J/\psi$ -007] data: on their domain of coverage, those data are entirely consistent with our  $\mathbb{P}$ -dyn reaction model. Reviewing Figs. 14 B, C, it is evident that, as one would expect, the importance of any nondiffractive contributions to the differential cross section diminishes with increasing  $E_\gamma$ .

Our predictions for the  $W$  dependence of the total  $\gamma p \rightarrow J/\psi p$  photoproduction cross section are displayed in Fig. 15. As explained in Ref. [9], the  $\mathbb{P}$ -dyn reaction model provides a good description of all available data [40, H1 2000], [33, ZEUS 2002], [98, LHCb 2014], [20, GlueX 2023], [21, LHCb 2024], and pre-2000 [92, 99–104], which today covers a domain from threshold to  $W \simeq 2 \text{ TeV}$ . Near threshold, a realistic description of the  $\gamma \rightarrow q\bar{q} + \mathbb{P} \rightarrow V$  transition matrix element in Fig. 1 is crucial in achieving agreement with data: the  $\mathbb{P}$ -am model fails on this domain, becoming viable only on  $W \gtrsim 5 \text{ GeV}$ .

Emulating Ref. [9, Fig. 6], Fig. 15 also includes comparisons with other reaction models. Regarding the GPD model, the best-fit curve from Ref. [93] is drawn: the framework is inapplicable on  $W \gtrsim 5 \text{ GeV}$ ; hence, it cannot meet a requirement for providing a uniformly applicable approach. Furthermore, even on the subdomain of assumed applicability, the description of [20, 94, GlueX] data does not match that produced by the  $\mathbb{P}$ -dyn reaction model, *viz.* the approach advocated herein. These facts further impair attempts to connect near threshold  $J/\psi$  photoproduction data with the in-proton gluon GPD.

On the other hand, the reaction model in Ref. [34], delivers a good description of available total cross-section data on the domain  $W_{\text{th}}^{J/\psi} < W < 300 \text{ MeV}$ . In this

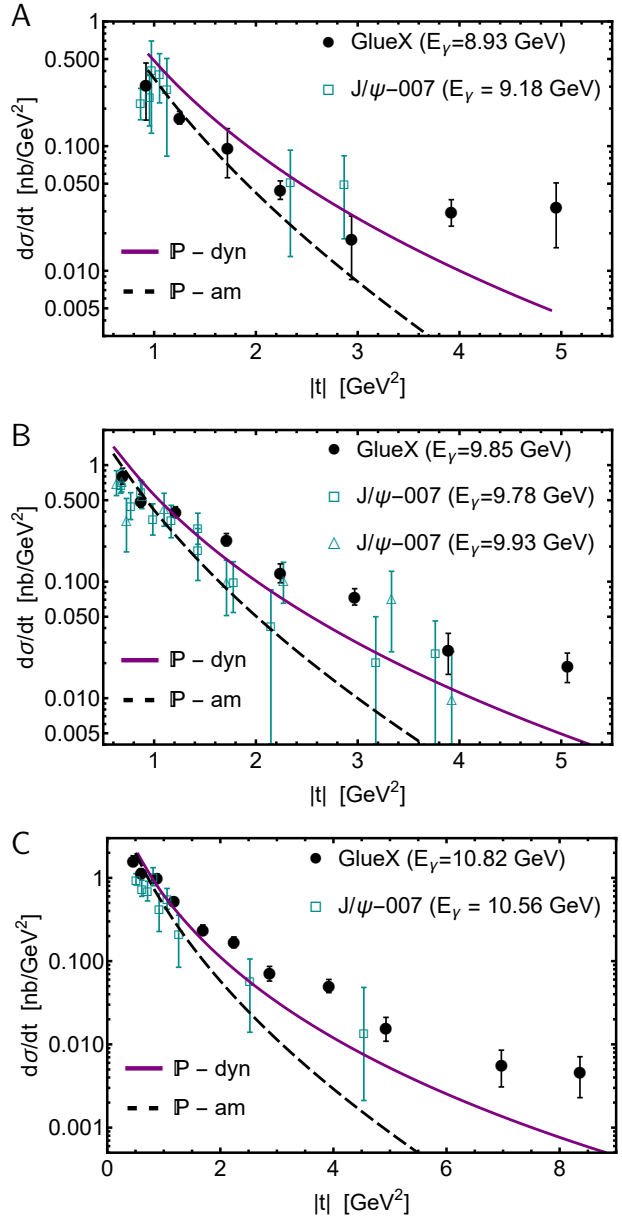


Fig. 14:  $|t|$  dependence of  $J/\psi$  photoproduction differential cross sections near threshold,  $W_{\text{th}}^{J/\psi} = 4.04 \text{ GeV}$ . Solid purple curve –  $\mathbb{P}$ -dyn; dotted purple –  $\mathbb{P}$ -am. The different panels depict, respectively photon energies  $E_\gamma = 8.93, 9.85, 10.82 \text{ GeV}$ , which correspond to  $W = 4.2, 4.4, 4.6 \text{ GeV}$ . Data: black circles – [20, GlueX]; cyan squares and triangles – [95,  $J/\psi$ -007].

case, considering also the model's results for the differential cross section – see Fig. 12, it is the link drawn between such agreement and dominance of FSIs near threshold that is debatable. The connection relies on a particular choice for the Pomeron trajectory. If one instead uses the trajectory we have described – Table 1 – Row 3 – namely, that associated with  $\mathbb{P}$ -dyn, then an

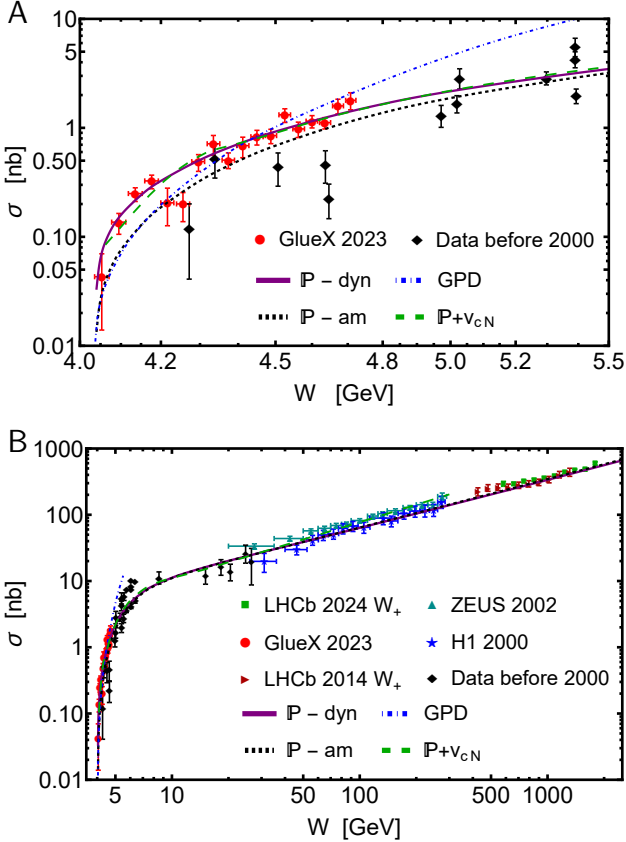


Fig. 15:  $W$  dependence of total  $J/\psi$  photoproduction cross section,  $W_{\text{th}}^{J/\psi} = 4.04$  GeV. Panel A. Near-threshold region,  $W_{\text{th}}^{J/\psi} < W < 5.5$  GeV. Panel B. Entire coverage of available data,  $W_{\text{th}}^{J/\psi} < W < 2$  TeV. Solid purple curve –  $\mathbb{P}$ -dyn; dashed black –  $\mathbb{P}$ -am. Data: blue stars – [40, H1 2000]; cyan up-triangles – [33, ZEUS 2002]; red right-triangles – [98, LHCb 2014]; red circles – [20, GlueX 2023]; green squares – [21, LHCb 2024]; black diamonds – pre-2000 [92, 99–104].

equivalent description of data is possible without calling upon FSIs.

#### 5.4 $\Upsilon$ photoproduction

To complete the picture, it remains only to consider  $\Upsilon$  photoproduction, the threshold for which is  $W_{\text{th}}^{\Upsilon} = 10.40$  GeV. Today, there are no differential cross section data and total cross sections are only available on  $100 \lesssim W/\text{GeV} \lesssim 2000$ . Owing to the large mass of the valence  $b, \bar{b}$  quarks, there are attempts to employ perturbative QCD concepts as the basis for explaining available data; see, *e.g.*, Refs. [105–107]. As we shall see, this is by no means mandatory.

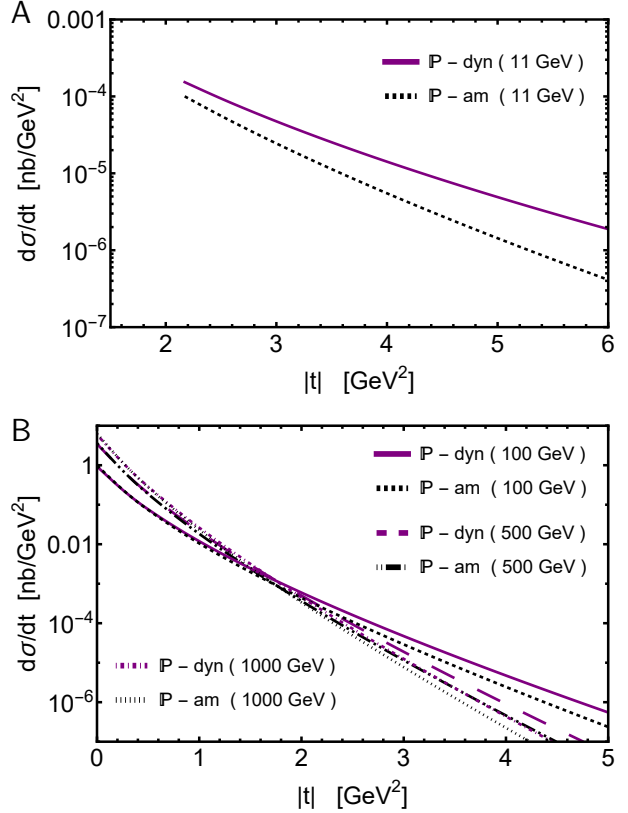


Fig. 16:  $|t|$  dependence of differential cross section for  $\Upsilon$  photoproduction. Panel A.  $W = 11$  GeV. Panel B.  $\mathbb{P}$ -dyn: solid purple –  $W = 100$  GeV; long-dashed purple – 500 GeV; dot-dashed purple – 1 TeV.  $\mathbb{P}$ -am: dashed black –  $W = 100$  GeV; dot-dot-dashed black – 500 GeV; dotted black – 1 TeV.

Our predictions for the  $\gamma p \rightarrow \Upsilon p$  differential cross section are drawn in Fig. 16. Owing to the large  $\Upsilon$  mass,  $t_{\min} \approx 2.2$  GeV $^2$  near-threshold. Naturally, it diminishes with increasing  $W$ . Regarding Fig. 16 A, it is apparent that even for  $\Upsilon$  photoproduction, the dynamical quark loop in Fig. 1 plays a material role near threshold. However, as in the other cases considered herein, precise data would be necessary to distinguish between competing reaction mechanisms on this domain. Turning to Fig. 16 B, it is evident that, with increasing  $W$ , the Pomeron trajectory dominates the differential cross section on the diffractive domain. It is worth stressing here that we use the same Pomeron trajectory for both  $J/\psi$  and  $\Upsilon$  production.

The total cross section for  $\Upsilon$  photoproduction is displayed in Fig. 17. The  $\mathbb{P}$ -dyn and  $\mathbb{P}$ -am reaction models yield equivalent results; so one may conclude that on the domain covered by extant experiments, simple Pomeron exchange is sufficient to describe the data. Precise data closer to threshold would be valuable. This

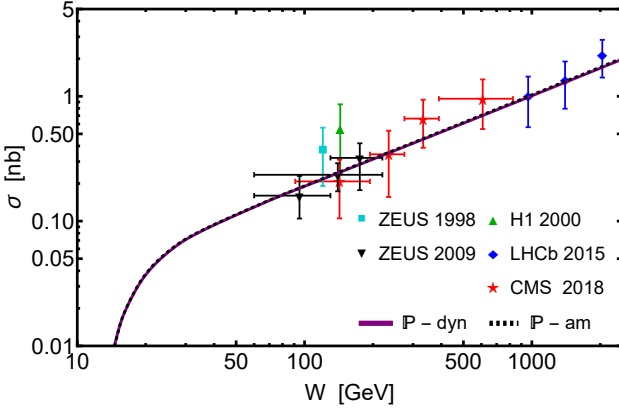


Fig. 17:  $W$  dependence of total cross section for  $\gamma$  photoproduction, with  $W_{\text{th}}^{\gamma} = 10.40$  GeV. Solid purple curves –  $\mathbb{P}$ –dyn; dashed black –  $\mathbb{P}$ –am. Data: cyan squares – [39, ZEUS 1998]; green up-triangles – [40, H1 2000]; black down-triangles – [41, ZEUS 2009]; blue diamonds – [42, LHCb 2015]; red stars – [43, CMS 2018].

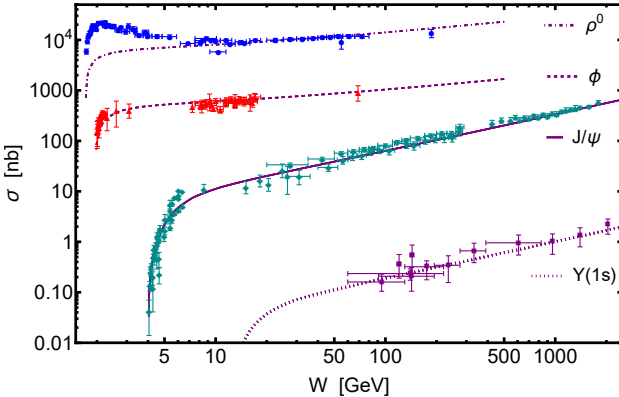


Fig. 18: Total cross sections for all vector meson photoproduction reactions considered herein. Each curve is the associated  $\mathbb{P}$ –dyn prediction. The data sources are recorded in Figs. 4, 6, 12, 17.

may be expected from experiments at future electron ion colliders [17–19].

## 6 Results: power-law behavior of vector meson photoproduction cross sections

Figure 18 records the total cross sections for all vector meson photoproduction reactions considered herein, depicting  $\mathbb{P}$ –dyn predictions vs. data. In the analysis of data, it is common to report power-law exponents that characterise the large- $W$  behaviour of such cross sections. They are typically extracted using one of the

Table 3: Power-law exponents extracted using Eqs. (23) via least-squares fits to  $W$  dependence of  $\rho$ ,  $\phi$ ,  $J/\psi$ ,  $\Upsilon$  photoproduction cross sections as calculated using: Panel A –  $\mathbb{P}$ –dyn reaction model; and Panel B –  $\mathbb{P}$ –am. When employing Eq. (23a), only  $W > W_{\text{min}}$  data can be used, *i.e.*, data well above threshold. Herein:  $W_{\text{min}}^{\rho, \phi} = 5$  GeV;  $W_{\text{min}}^{J/\psi} = 10$  GeV;  $W_{\text{min}}^{\Upsilon} = 35$  GeV. Empirical values taken from Refs. [43, 70, 108, 109]. Somewhat unrefined empirical estimates are also available in Ref. [36, Fig. 1].

A		Eq. (23a)		Eq. (23b)		Expt.
$V$	$X/\text{nb}$	$\epsilon$	$\sigma_P/\text{nb}$	$\epsilon$	$\epsilon$	
$\rho^0$	4076	0.27	5611	0.21	$0.17 \pm 0.01^{+0.04}_{-0.03}$	
$\phi$	234.2	0.26	430.0	0.20	$\approx \epsilon_{\rho}$ [36, 108]	
$J/\psi$	2.136	0.73	2.178	0.73	$0.67 \pm 0.03$	
$\Upsilon$	0.0064	0.73	0.0066	0.73	$0.77 \pm 0.14$	

B		Eq. (23a)		Eq. (23b)		Expt.
$V$	$X/\text{nb}$	$\epsilon$	$\sigma_P/\text{nb}$	$\epsilon$	$\epsilon$	
$\rho^0$	3368	0.32	4151	0.27	$0.17 \pm 0.01^{+0.04}_{-0.03}$	
$\phi$	268.6	0.30	343.7	0.25	$\approx \epsilon_{\rho}$ [36, 108]	
$J/\psi$	2.099	0.74	2.139	0.74	$0.67 \pm 0.03$	
$\Upsilon$	0.0067	0.74	0.0066	0.73	$0.77 \pm 0.14$	

following formulae [26, 110]:

$$\sigma(W) = XW^{\epsilon}, \quad (23a)$$

$$\sigma(W) = \sigma_P \left[ 1 - \frac{(m_p + m_V)^2}{W^2} \right]^2 W^{\epsilon}. \quad (23b)$$

*N.B.* Equation (23b) is applicable  $\forall W$ , whereas Eq. (23a) can only be used on some domain well above threshold, *viz.*  $W > W_{\text{min}} \gg W_{\text{th}}$ .

For the  $\mathbb{P}$ –dyn reaction model, values of the fitting parameters are listed in Table 3 A and compared with empirical inferences. In all cases, the comparison is good when using Eq. (23b); and Eq. (23a) serves well for heavy mesons.

Employing analogous  $\mathbb{P}$ –am results from Figs. 4, 6, 14, 16, one obtains the exponents listed in Table 3 B. In this case, a favourable comparison with empirical inferences is only achieved for heavy mesons,  $V = J/\psi, \Upsilon$ .

In the standard Pomeron-alone framework, the exponent should be [26]:

$$\epsilon \approx 4[\alpha_{\mathbb{P}}(0) - 1]. \quad (24)$$

Consideration of Eqs. (3), (7), (12) indicates that a better estimate is provided by the following formula:

$$\epsilon(t_{\text{min}}(W)) \approx 4[\alpha_{\mathbb{P}}(t_{\text{min}}(W)) - 1], \quad (25)$$

Table 4: VMD-based scattering lengths – Eq. (18) – inferred from near-threshold  $V$ -meson photoproduction differential cross sections calculated using the  $\mathbb{P}$ –dyn and  $\mathbb{P}$ –am reaction models.  $q_{th}$  is the photon momentum at threshold in the centre-of-mass frame. The value of  $|\alpha_{Vp}^{\text{VMD}}|$  was estimated in Ref. [62] by using near-threshold pseudodata created using the GPD model in Ref. [111], which is an earlier version of the GPD model discussed above [93]: the GPD reaction model delivers results that disagree with ours by an order of magnitude and more.

$V$	$m_V/\text{GeV}$	$q_{th}/\text{GeV}$	$\Gamma_{V \rightarrow e^+ e^-}/\text{keV}$	$ \alpha_{Vp}^{\text{dyn}} /\text{fm}$	$ \alpha_{Vp}^{\text{am}} /\text{fm}$	$ \alpha_{Vp}^{\text{VMD}} /\text{fm}$
$\rho^0$	0.775	0.6	6.97	0.136	0.072	$0.23 \pm 0.03$ [63]
$\phi^0$	1.019	0.75	1.27	0.087	0.048	$0.063 \pm 0.010$ [61]
$J/\psi$	3.097	1.91	5.53	$3.08 \times 10^{-3}$	$1.88 \times 10^{-3}$	$3.08(55) \times 10^{-3}$ [60]
$\Upsilon$	9.46	5.16	1.34	$5.87 \times 10^{-5}$	$1.86 \times 10^{-5}$	$0.51(3) \times 10^{-3}$ [62]

where  $|t_{\min}(W)|$  decreases with increasing  $W$ . Notwithstanding Eq. (25), phenomenological analyses of data use Eqs. (23); so return a  $W$ -independent exponent, which must therefore be some mean- $\epsilon$ , averaged over the measurement domain. Working from Table 1, Eq. (24) yields  $\epsilon_\rho = \epsilon_\phi = 0.4$  and  $\epsilon_{J/\psi} = \epsilon_\Upsilon = 0.8$ . Evidently, considering Table 3, whilst Eq. (24) is a fair approximation for heavy meson data,  $V = J/\psi, \Upsilon$ , it delivers a poor estimate for light meson data,  $V = \rho, \phi$ .

We note that both the  $\mathbb{P}$ –dyn and  $\mathbb{P}$ –am reaction models deliver exponents in qualitative agreement with Eqs. (24), (25): since  $\alpha_0^\rho = \alpha_0^\phi$ ,  $\alpha_0^{J/\psi} = \alpha_0^\Upsilon$  in Table 1, and  $|t_{\min}|$  is small, then  $\epsilon_\rho \approx \epsilon_\phi$  and  $\epsilon_{J/\psi} \approx \epsilon_\Upsilon$ .

On the other hand, whereas there is quantitative agreement between Eq. (24) and both  $\mathbb{P}$ –dyn and  $\mathbb{P}$ –am predictions for  $V = J/\psi, \Upsilon$ , this is not the case for  $V = \rho, \phi$ . An explanation is found in comparing the predictions in Table 3 A with those in Table 3 B. The  $\mathbb{P}$ –am model – see Fig. 2 – ignores the quark + antiquark transition loop in Fig. 1. It only keeps some  $t$ -dependence via Eq. (15); hence  $\mathbb{P}$ –am is closer to a pure Pomeron description. Consequently, with less additional interaction structure, the  $V = \rho, \phi$   $\mathbb{P}$ –am exponents are closer to those anticipated from Eq. (24). A small mean value of  $|\bar{t}_{\min}| = 0.061 \text{ GeV}^2 \approx |t_{\min}^\rho|/4$  in Eq. (25) yields  $\epsilon(\bar{t}_{\min}) = 0.32$ , matching the value in Table 3 B.

This discussion highlights that structure in the  $\gamma \rightarrow V$  transition component of the  $\gamma p \rightarrow Vp$  matrix element has an impact on the exponent value. Naturally, the effects are greater for the  $\mathbb{P}$ –dyn reaction model and, indeed, are just what is needed to deliver agreement with the empirically deduced exponent for light mesons. As we have shown above, such corrections diminish at the typically larger  $W$  values associated with  $V = J/\psi, \Upsilon$  photoproduction.

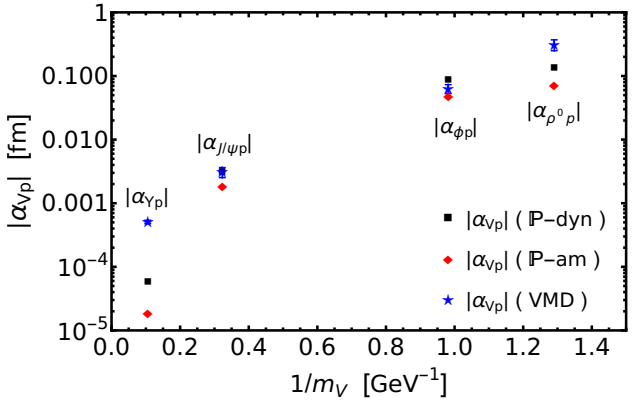


Fig. 19: VMD-based scattering lengths – Eq. (18) – inferred from near-threshold vector meson photoproduction differential cross sections. Pictorial representation of the results listed in Table 4.

## 7 Results: near-threshold slope parameter / vector meson-proton scattering lengths

As noted in Sect. 4, despite its weaknesses [24], VMD remains a widely used phenomenological tool; and within that framework, there is a simple relationship between the differential cross section for  $\gamma p \rightarrow Vp$  and the  $V - p$  scattering length, namely, Eq. (18). Our prediction for the  $\gamma p \rightarrow Vp$  differential cross section is given in Eq. (7) and this is the formula we used above to calculate all results.

Here, for the sake of a comparison between our predictions and the model-specific VMD-values of meson-proton scattering lengths inferred in Refs. [60–63], we equate our near-threshold results with Eq. (18) to arrive at a crude estimate of  $|\alpha_{Vp}|$ . The results are listed in Table 4 and plotted in Fig. 19. The differences between  $\mathbb{P}$ –dyn and  $\mathbb{P}$ –am predictions again highlight the importance of the dynamical quark loop – Fig. 1 – near threshold. It is worth recording the following pattern in our predictions:

$$|\alpha_{\Upsilon p}| \ll |\alpha_{J/\psi p}| \ll |\alpha_{\phi p}| < |\alpha_{\rho^0 p}|. \quad (26)$$

The  $\mathbb{P}$ -dyn results may be described by

$$|\alpha_{Vp}| \approx a_0/m_V^3, \quad a_0 = (0.41 \text{ GeV})^3 \text{ fm.} \quad (27)$$

As observed in Sect. 4, one need not interpret  $|\alpha_{Vp}|$  as the  $V - p$  scattering length; instead, it can simply be viewed as a near-threshold slope parameter, in which case the value has objective utility as a comparison between theory and experiment.

Regarding  $V = \rho^0$ , there is qualitative agreement between our near-threshold slope and that associated with available data. One should not expect better because, as explained in Sect. 5.1, nondiffractive processes are important for  $\rho$ -meson photoproduction and the empirically inferred value is based on pseudodata [63]. Turning to  $\phi$  photoproduction, Sect. 5.2 describes good agreement between our predictions and data, so our value for the  $\phi$  slope parameter should be reliable. Hence, the agreement with data is good, especially when one considers the scatter in available near threshold data; see Figs. 7–10. Owing to the heightened interest in  $J/\psi$  photoproduction, a good deal of modern data is available near threshold. Our prediction for the associated slope parameter agrees well with the value deduced from the new data.

The outlier in Table 4 is the slope parameter associated with near threshold  $\Upsilon$  photoproduction. In our view, given its success with  $J/\psi$  photoproduction, the  $\mathbb{P}$ -dyn reaction model should be reliable for  $\Upsilon$ , too. However, its prediction is an order of magnitude and more smaller than that listed in Ref. [62]. We judge that the explanation for this mismatch is straightforward. The estimate in Ref. [62] is based on pseudodata produced near threshold using the GPD model in Ref. [111], which is an earlier version of the GPD model discussed above [93]. As observed in Sect. 5.3 and Ref. [9], the GPD model provides a poor representation of near-threshold  $J/\psi$  data; so one should not expect it to be reliable for  $\Upsilon$  photoproduction. Data from future electron ion collider experiments may be expected to resolve this issue. Meanwhile, we present our prediction as a solidly benchmarked estimate.

## 8 Summary and perspective

We described and employed a reaction model,  $\mathbb{P}$ -dyn, for  $\gamma + p \rightarrow V + p$  photoproduction,  $V = \rho^0, \phi, J/\psi, \Upsilon$ , that exposes the quark-antiquark content of the dressed photon in making the transition  $\gamma \rightarrow q\bar{q} + \mathbb{P} \rightarrow V$ , where  $q$  depends on  $V$ , and couples the intermediate  $q\bar{q}$  system to the proton's valence quarks via Pomeron exchange [Fig. 1]. The parameters in this model are those characterising the Pomeron trajectories for light (two)

and heavy mesons (two) and the Pomeron-quark couplings (four). With those parameters fitted to high- $W$  data [Sect. 2.4],  $\mathbb{P}$ -dyn provides a uniformly good description of a large number of differential and total cross-sections for  $V$ -meson photoproduction from the proton on the entire kinematic ranges measured to date [Sect. 5]. In all cases, the quality of the description is as good as or better than that provided by alternative models. The quark loop in Fig. 1 plays a key role in the success of the  $\mathbb{P}$ -dyn reaction description.

There is one caveat, however. Namely, as one moves away from the forward limit, nondiffractive mechanisms can play a role in the photoproduction process. Since the  $\rho^0$  contains valence degrees of freedom in common with the proton, that is most apparent for  $\rho^0$  production. In this case, the  $\mathbb{P}$ -dyn reaction model is insufficient on a domain that extends from threshold,  $W_{\text{th}}^\rho$ , to  $W \approx 5 \text{ GeV}$ , where  $W$  is the centre of mass energy [Fig. 4].

Working with  $\mathbb{P}$ -dyn predictions, we extracted the power-law exponents that are often used empirically to characterise the large- $W$  behaviour of total cross sections for  $\gamma + p \rightarrow V + p$  photoproduction [Sect. 6]. Our results agree well with phenomenological inferences from data. For light mesons, the exponents do not take the values suggested by simple Pomeron pictures. Again, the quark loop in Fig. 1 plays a key role in these outcomes.

We also used the  $\mathbb{P}$ -dyn predictions to extract near-threshold slope parameters that can be used to characterise the differential cross sections for  $\gamma + p \rightarrow V + p$  photoproduction [Sect. 7]. Owing to the role of nondiffractive processes, we judge that the  $\rho^0$  value is underestimated. On the other hand, the predictions for  $V = \phi, J/\psi, \Upsilon$  are solidly benchmarked; hence, should serve as realistic estimates.

Acknowledging the  $\rho$ -meson caveat, our  $\mathbb{P}$ -dyn reaction model delivers a uniformly good, unified description of forward  $V = \rho^0, \phi, J/\psi, \Upsilon$  meson photoproduction from relevant thresholds to very high energies. A key to this success is a realistic nonperturbative description of the  $\gamma \rightarrow V$  transition, which is especially important near threshold but also plays a role at higher energies. Apart from the interaction dynamics expressed in treating that loop, the Pomeron provides the only link to “gluon” physics in the reaction model and, so far is now known, that mechanism is unrelated to in-proton gluon distributions. Hence, at present, any attempt to constrain such distributions using near-threshold  $\gamma + p \rightarrow V + p$  photoproduction data is unjustified. The desire to make such interpretations should be restrained whilst development of reaction models continues and higher precision data are accumulated. One may antic-

ipate that subsequent mutual feedback could lead to a well constrained phenomenology which may be employed in understanding  $\gamma + p \rightarrow V + p$  processes and forging a tight link between the associated data and proton properties.

**Acknowledgements** We are grateful to Z.-F. Cui (崔著钫), T.-S. H. Lee, V. I. Mokeev, I. Strakovsky and J.-J. Wu for discussions and suggestions. Work supported by: National Natural Science Foundation of China, grant no. 12135007.

**Data Availability Statement** Data will be made available on reasonable request. [Authors' comment: All information necessary to reproduce the results described herein is contained in the material presented above.]

**Code Availability Statement** Code/software will be made available on reasonable request. [Authors' comment: No additional remarks.]

## Appendix A: Tensor structure of the $\gamma \rightarrow V$ transition

The essentially dynamical component of the reaction model, *viz.* the  $\gamma \rightarrow q\bar{q} + \mathbb{P} \rightarrow V$  transition matrix element, has the tensor structure apparent in Eq. (20). The tensors take the following form:

$$\tau_{\mu\nu\alpha}^1(q, P) = q_\alpha R_{\mu\nu}, \quad (\text{A.1a})$$

$$\tau_{\mu\nu\alpha}^2(q, P) = P_\alpha R_{\mu\nu}, \quad (\text{A.1b})$$

$$\tau_{\mu\nu\alpha}^3(q, P) = q_\alpha q_\nu S_\nu, \quad (\text{A.1c})$$

$$\tau_{\mu\nu\alpha}^4(q, P) = P_\alpha q_\mu S_\nu, \quad (\text{A.1d})$$

$$\tau_{\mu\nu\alpha}^5(q, P) = q_\alpha P_\mu S_\nu, \quad (\text{A.1e})$$

$$\tau_{\mu\nu\alpha}^6(q, P) = P_\mu T_{\alpha\nu}, \quad (\text{A.1f})$$

$$\tau_{\mu\nu\alpha}^7(q, P) = q_\mu T_{\alpha\nu}, \quad (\text{A.1g})$$

$$\tau_{\mu\nu\alpha}^8(q, P) = \delta_{\mu\alpha} S_\nu, \quad (\text{A.1h})$$

$$\tau_{\mu\nu\alpha}^9(q, P) = P_\alpha P_\mu S_\nu, \quad (\text{A.1i})$$

where

$$R_{\mu\nu} = \delta_{\mu\nu} - P_\mu P_\nu / P^2, \quad (\text{A.2a})$$

$$S_\nu = q_\nu - P_\nu P \cdot q / P^2. \quad (\text{A.2b})$$

## References

1. L. Baksay, et al., Measurement of the Proton Proton Total Cross-Section and Small Angle Elastic Scattering at ISR Energies, *Nucl. Phys. B* 141 (1978) 1–28, [Erratum: *Nucl. Phys. B* 148 (1979) 538–539].
2. L. L. Foldy, R. F. Peierls, Isotopic Spin of Exchanged Systems, *Phys. Rev.* 130 (1963) 1585–1589.
3. S. Donnachie, H. G. Dosch, O. Nachtmann, P. Landshoff, *Pomeron physics and QCD*, vol. 19 of *Cambridge Monogr. Part. Phys. Nucl. Phys. Cosmol.*, Cambridge University Press, 2004.
4. V. N. Gribov, The theory of complex angular momenta: Gribov lectures on theoretical physics, Cambridge Monographs on Mathematical Physics, Cambridge University Press, 2007.
5. J. R. Forshaw, D. A. Ross, *Quantum chromodynamics and the pomeron*, vol. 9, Cambridge University Press, Cambridge, UK, 2011.
6. H. B. Meyer, M. J. Teper, Glueball Regge trajectories and the pomeron: A Lattice study, *Phys. Lett. B* 605 (2005) 344–354.
7. H. Boschi-Filho, N. R. F. Braga, H. L. Carrion, Glueball Regge trajectories from gauge/string duality and the Pomeron, *Phys. Rev. D* 73 (2006) 047901.
8. M. A. Pichowsky, T. S. H. Lee, Exclusive diffractive processes and the quark substructure of mesons, *Phys. Rev. D* 56 (1997) 1644–1662.
9. L. Tang, Y.-X. Yang, Z.-F. Cui, C. D. Roberts,  $J/\psi$  photoproduction: Threshold to very high energy, *Phys. Lett. B* 856 (2024) 138904.
10. G. Eichmann, H. Sanchis-Alepuz, R. Williams, R. Alkofer, C. S. Fischer, Baryons as relativistic three-quark bound states, *Prog. Part. Nucl. Phys.* 91 (2016) 1–100.
11. V. D. Burkert, C. D. Roberts, Roper resonance: Toward a solution to the fifty-year puzzle, *Rev. Mod. Phys.* 91 (2019) 011003.
12. C. D. Roberts, D. G. Richards, T. Horn, L. Chang, Insights into the emergence of mass from studies of pion and kaon structure, *Prog. Part. Nucl. Phys.* 120 (2021) 103883.
13. D. Binosi, Emergent Hadron Mass in Strong Dynamics, *Few Body Syst.* 63 (2) (2022) 42.
14. M. Ding, C. D. Roberts, S. M. Schmidt, Emergence of Hadron Mass and Structure, *Particles* 6 (1) (2023) 57–120.
15. M. N. Ferreira, J. Papavassiliou, Gauge Sector Dynamics in QCD, *Particles* 6 (1) (2023) 312–363.
16. P. Achenbach, D. S. Carman, R. W. Gothe, K. Joo, V. I. Mokeev, C. D. Roberts, Electroexcitation of Nucleon Resonances and the Emergence of Hadron Mass, *Symmetry* 17 (7) (2025) 1106.
17. X. Chen, F.-K. Guo, C. D. Roberts, R. Wang, Selected Science Opportunities for the EicC, *Few Body Syst.* 61 (2020) 43.
18. D. P. Anderle, et al., Electron-ion collider in China, *Front. Phys. (Beijing)* 16 (6) (2021) 64701.
19. R. Abdul Khalek, et al., Science Requirements and Detector Concepts for the Electron-Ion Collider:

EIC Yellow Report, Nucl. Phys. A 1026 (2022) 122447.

20. S. Adhikari, et al., Measurement of the  $J/\psi$  photoproduction cross section over the full near-threshold kinematic region, Phys. Rev. C 108 (2) (2023) 025201.
21. R. Aaij, et al., Measurement of exclusive  $J/\psi$  and  $\psi(2S)$  production at  $\sqrt{s} = 13$  TeV, SciPost Phys. 18 (2) (2025) 071.
22. A. Donnachie, P. V. Landshoff, Elastic Scattering and Diffraction Dissociation, Nucl. Phys. B 244 (1984) 322.
23. A. Donnachie, P. V. Landshoff, Exclusive rho Production in Deep Inelastic Scattering, Phys. Lett. B 185 (1987) 403.
24. Y.-Z. Xu, S. Chen, Z.-Q. Yao, D. Binosi, Z.-F. Cui, C. D. Roberts, Vector-meson production and vector meson dominance, Eur. Phys. J. C 81 (2021) 895.
25. J. S. Ball, T.-W. Chiu, Analytic Properties of the Vertex Function in Gauge Theories. 1, Phys. Rev. D 22 (1980) 2542–2549.
26. A. Donnachie, P. V. Landshoff, Total cross-sections, Phys. Lett. B 296 (1992) 227–232.
27. P. D. B. Collins, An Introduction to Regge Theory and High Energy Physics, Cambridge Monographs on Mathematical Physics, Cambridge University Press, 1977.
28. A. C. Irving, R. P. Worden, Regge Phenomenology, Phys. Rept. 34 (1977) 117–231.
29. T. S. H. Lee, S. Sakinah, Y. Oh, Models of  $J/\Psi$  photo-production reactions on the nucleon, Eur. Phys. J. A 58 (12) (2022) 252.
30. S.-X. Qin, C. D. Roberts, S. M. Schmidt, Poincaré-covariant analysis of heavy-quark baryons, Phys. Rev. D 97 (2018) 114017.
31. M. B. Hecht, C. D. Roberts, S. M. Schmidt, Valence-quark distributions in the pion, Phys. Rev. C 63 (2001) 025213.
32. S. Navas, et al., Review of particle physics, Phys. Rev. D 110 (3) (2024) 030001.
33. S. Chekanov, et al., Exclusive photoproduction of  $J/\psi$  mesons at HERA, Eur. Phys. J. C 24 (2002) 345–360.
34. S. Sakinah, T. S. H. Lee, H.-M. Choi, Dynamical Model of  $J/\Psi$  photo-production on the nucleon – arXiv:2403.01958 [nucl-th].
35. A. I. Titov, Y.-s. Oh, S. N. Yang, T. Morii, Photoproduction of phi meson from proton: Polarization observables and the strangeness in the nucleon, Phys. Rev. C 58 (1998) 2429–2449.
36. M. Capua, Vector Mesons and DVCS at HERA, in: 3rd International Workshop on Multiple Partonic Interactions at the LHC, 137–143, 2012.
37. M. Derrick, et al., Measurement of elastic  $\rho^0$  photoproduction at HERA, Z. Phys. C 69 (1995) 39–54.
38. M. Derrick, et al., Measurement of elastic  $\phi$  photoproduction at HERA, Phys. Lett. B 377 (1996) 259–272.
39. J. Breitweg, et al., Measurement of elastic Upsilon photoproduction at HERA, Phys. Lett. B 437 (1998) 432–444.
40. C. Adloff, et al., Elastic photoproduction of  $J/\psi$  and  $\Upsilon$  mesons at HERA, Phys. Lett. B 483 (2000) 23–35.
41. S. Chekanov, et al., Exclusive photoproduction of upsilon mesons at HERA, Phys. Lett. B 680 (2009) 4–12.
42. R. Aaij, et al., Measurement of the exclusive  $\Upsilon$  production cross-section in pp collisions at  $\sqrt{s} = 7$  TeV and 8 TeV, JHEP 09 (2015) 084.
43. A. M. Sirunyan, et al., Measurement of exclusive  $\Upsilon$  photoproduction from protons in pPb collisions at  $\sqrt{s_{NN}} = 5.02$  TeV, Eur. Phys. J. C 79 (3) (2019) 277, [Erratum: Eur. Phys. J. C 82, 343 (2022)].
44. C. D. Roberts, Strong QCD and Dyson-Schwinger Equations, IRMA Lect. Math. and Theor. Phys. 21 (2015) 356–458.
45. A. Bashir, L. Chang, I. C. Cloet, B. El-Bennich, Y.-X. Liu, C. D. Roberts, P. C. Tandy, Collective perspective on advances in Dyson-Schwinger Equation QCD, Commun. Theor. Phys. 58 (2012) 79–134.
46. K. Raya, A. Bashir, D. Binosi, C. D. Roberts, J. Rodríguez-Quintero, Pseudoscalar Mesons and Emergent Mass, Few Body Syst. 65 (2) (2024) 60.
47. H. J. Munczek, Dynamical chiral symmetry breaking, Goldstone's theorem and the consistency of the Schwinger-Dyson and Bethe-Salpeter Equations, Phys. Rev. D 52 (1995) 4736–4740.
48. A. Bender, C. D. Roberts, L. von Smekal, Goldstone Theorem and Diquark Confinement Beyond Rainbow- Ladder Approximation, Phys. Lett. B 380 (1996) 7–12.
49. P. Maris, C. D. Roberts,  $\pi$  and  $K$  meson Bethe-Salpeter amplitudes, Phys. Rev. C 56 (1997) 3369–3383.
50. A. Bashir, A. Raya, S. Sánchez-Madrigal, C. D. Roberts, Gauge invariance of a critical number of flavours in QED3, Few Body Syst. 46 (2009) 229–237.
51. S.-X. Qin, L. Chang, Y.-X. Liu, C. D. Roberts, D. J. Wilson, Interaction model for the gap equation, Phys. Rev. C 84 (2011) 042202(R).

52. D. Binosi, L. Chang, J. Papavassiliou, C. D. Roberts, Bridging a gap between continuum-QCD and *ab initio* predictions of hadron observables, *Phys. Lett. B* 742 (2015) 183–188.

53. L. Chang, Y.-X. Liu, C. D. Roberts, Y.-M. Shi, W.-M. Sun, H.-S. Zong, Chiral susceptibility and the scalar Ward identity, *Phys. Rev. C* 79 (2009) 035209.

54. S.-X. Qin, C. D. Roberts, Impressions of the Continuum Bound State Problem in QCD, *Chin. Phys. Lett.* 37 (12) (2020) 121201.

55. M. Chen, M. Ding, L. Chang, C. D. Roberts, Mass-dependence of pseudoscalar meson elastic form factors, *Phys. Rev. D* 98 (2018) 091505(R).

56. M. Ding, K. Raya, A. Bashir, D. Binosi, L. Chang, M. Chen, C. D. Roberts,  $\gamma^* \gamma \rightarrow \eta, \eta'$  transition form factors, *Phys. Rev. D* 99 (2019) 014014.

57. Y.-Z. Xu, D. Binosi, Z.-F. Cui, B.-L. Li, C. D. Roberts, S.-S. Xu, H.-S. Zong, Elastic electromagnetic form factors of vector mesons, *Phys. Rev. D* 100 (2019) 114038.

58. M. S. Bhagwat, A. Höll, A. Krassnigg, C. D. Roberts, P. C. Tandy, Aspects and consequences of a dressed-quark-gluon vertex, *Phys. Rev. C* 70 (2004) 035205.

59. Z.-Q. Yao, D. Binosi, Z.-F. Cui, C. D. Roberts, Semileptonic  $B_c \rightarrow \eta_c, J/\psi$  transitions, *Phys. Lett. B* 818 (2021) 136344.

60. I. Strakovsky, D. Epifanov, L. Pentchev,  $J/\psi p$  scattering length from GlueX threshold measurements, *Phys. Rev. C* 101 (4) (2020) 042201.

61. I. I. Strakovsky, L. Pentchev, A. Titov, Comparative analysis of  $\omega p$ ,  $\phi p$ , and  $J/\psi p$  scattering lengths from A2, CLAS, and GlueX threshold measurements, *Phys. Rev. C* 101 (4) (2020) 045201.

62. I. I. Strakovsky, W. J. Briscoe, L. Pentchev, A. Schmidt, Threshold Upsilon-meson photoproduction at the EIC and EicC, *Phys. Rev. D* 104 (7) (2021) 074028.

63. I. I. Strakovsky, E. L. Isupov, V. Mokeev, A. Schmidt,  $\rho$ -Meson Nucleon Scattering Length from CLAS Threshold Photoproduction Measurements – arXiv:2509.04672 [nucl-th].

64. W. Struczinski, et al., Study of photoproduction on hydrogen in a streamer chamber with tagged photons for  $1.6 \text{ GeV} < E_\gamma < 6.3 \text{ GeV}$  Topological and reaction cross sections, *Nucl. Phys. B* 108 (1976) 45–74.

65. D. Aston, et al., Photoproduction of  $\rho^0$  and  $\omega$  on Hydrogen at Photon Energies of 20-GeV to 70-GeV, *Nucl. Phys. B* 209 (1982) 56–76.

66. J. Park, M. Davier, I. Derado, D. E. C. Fries, F. F. Liu, R. F. Mozley, A. Odian, W. P. Swanson, F. Villa, D. Yount, THE REACTION  $\gamma p \rightarrow \rho^0 p$  AT 5.5-GeV TO 18-GeV, *Nucl. Phys. B* 36 (1972) 404.

67. J. Ballam, et al., STUDY OF HIGH-ENERGY PHOTOPRODUCTION WITH POSITRON ANNIHILATION RADIATION: I THREE PRONG EVENTS, *Phys. Rev. D* 5 (1972) 15.

68. R. M. Egloff, et al., Measurements of Elastic Rho and Phi Meson Photoproduction Cross-Sections on Protons from 30 GeV to 180 GeV, *Phys. Rev. Lett.* 43 (1979) 657.

69. S. Aid, et al., Elastic photoproduction of  $\rho^0$  mesons at HERA, *Nucl. Phys. B* 463 (1996) 3–32.

70. V. Andreev, et al., Measurement of Exclusive  $\pi^+ \pi^-$  and  $\rho^0$  Meson Photoproduction at HERA, *Eur. Phys. J. C* 80 (12) (2020) 1189.

71. V. I. Mokeev, et al., New Results from the Studies of the  $N(1440)1/2^+$ ,  $N(1520)3/2^-$ , and  $\Delta(1620)1/2^-$  Resonances in Exclusive  $ep \rightarrow e' p' \pi^+ \pi^-$  Electroproduction with the CLAS Detector, *Phys. Rev. C* 93 (2016) 025206.

72. T. Sato, T. S. H. Lee, Meson exchange model for  $\pi N$  scattering and  $\gamma N \rightarrow \pi N$  reaction, *Phys. Rev. C* 54 (1996) 2660–2684.

73. B.-G. Yu, T. K. Choi, K.-J. Kong, Features of  $\omega$  photoproduction off nucleon target at forward angles: dominance of  $\pi$  exchange with Regge cuts and scaling of differential cross-sections, *J. Phys. G* 46 (7) (2019) 075005.

74. J. Busenitz, et al., High-energy Photoproduction of  $\pi^+ \pi^- \pi^0$ ,  $K^+ K^-$ , and  $P\bar{P}$  States, *Phys. Rev. D* 40 (1989) 1–21.

75. B. Dey, C. A. Meyer, M. Bellis, M. Williams, Data analysis techniques, differential cross sections, and spin density matrix elements for the reaction  $\gamma p \rightarrow \phi p$ , *Phys. Rev. C* 89 (5) (2014) 055208, [Addendum: *Phys. Rev. C* 90, 019901 (2014)].

76. J. Ballam, et al., Vector Meson Production by Polarized Photons at 2.8-GeV, 4.7-GeV, and 9.3-GeV, *Phys. Rev. D* 7 (1973) 3150.

77. H. J. Besch, G. Hartmann, R. Kose, F. Krautschneider, W. Paul, U. Trinks, Photoproduction of phi mesons on protons at 2.0 gev, *Nucl. Phys. B* 70 (1974) 257–271.

78. H. J. Behrend, J. Bodenkamp, W. P. Hesse, W. A. McNeely, Jr., T. Miyachi, D. C. Fries, P. Heine, H. Hirschmann, A. Markou, E. Seitz, Elastic and Inelastic  $\phi$  - Photoproduction, *Nucl. Phys. B* 144 (1978) 22–60.

79. D. P. Barber, et al., A Study of Elastic Photoproduction of Low Mass  $K^+ K^-$  Pairs From Hydrogen

in the Energy Range 2.8-GeV to 4.8-GeV, *Z. Phys. C* 12 (1982) 1.

80. J. Barth, et al., Low-energy photoproduction of Phi mesons, *Eur. Phys. J. A* 17 (2003) 269–274.
81. T. Mibe, et al., Diffractive phi-meson photoproduction on proton near threshold, *Phys. Rev. Lett.* 95 (2005) 182001.
82. H. Seraydaryan, et al.,  $\phi$ -meson photoproduction on Hydrogen in the neutral decay mode, *Phys. Rev. C* 89 (5) (2014) 055206.
83. E. Anciant, et al., Photoproduction of phi(1020) mesons on the proton at large momentum transfer, *Phys. Rev. Lett.* 85 (2000) 4682–4686.
84. G. Krein, A. W. Thomas, K. Tsushima, Nuclear-bound quarkonia and heavy-flavor hadrons, *Prog. Part. Nucl. Phys.* 100 (2018) 161–210.
85. D. Kharzeev, Quarkonium interactions in QCD, *Proc. Int. Sch. Phys. Fermi* 130 (1996) 105–131.
86. C. D. Roberts, Perspective on the origin of hadron masses, *Few Body Syst.* 58 (2017) 5.
87. G. Krein, T. C. Peixoto, Femtoscopy of the Origin of the Nucleon Mass, *Few Body Syst.* 61 (4) (2020) 49.
88. G. Salmè, Explaining mass and spin in the visible matter: the next challenge, *J. Phys. Conf. Ser.* 2340 (1) (2022) 012011.
89. D. S. Carman, R. W. Gothe, V. I. Mokeev, C. D. Roberts, Nucleon Resonance Electroexcitation Amplitudes and Emergent Hadron Mass, *Particles* 6 (1) (2023) 416–439.
90. M.-L. Du, V. Baru, F.-K. Guo, C. Hanhart, U.-G. Meißner, A. Nefediev, I. Strakovsky, Deciphering the mechanism of near-threshold  $J/\psi$  photoproduction, *Eur. Phys. J. C* 80 (11) (2020) 1053.
91. P. Sun, X.-B. Tong, F. Yuan, Near threshold heavy quarkonium photoproduction at large momentum transfer, *Phys. Rev. D* 105 (5) (2022) 054032.
92. M. Derrick, et al., Measurement of the cross-section for the reaction  $\gamma p \rightarrow J/\psi p$  with the ZEUS detector at HERA, *Phys. Lett. B* 350 (1995) 120–134.
93. Y. Guo, X. Ji, Y. Liu, J. Yang, Updated analysis of near-threshold heavy quarkonium production for probe of proton's gluonic gravitational form factors, *Phys. Rev. D* 108 (3) (2023) 034003.
94. A. Ali, et al., First Measurement of Near-Threshold  $J/\psi$  Exclusive Photoproduction off the Proton, *Phys. Rev. Lett.* 123 (7) (2019) 072001.
95. B. Duran, et al., Determining the gluonic gravitational form factors of the proton, *Nature* 615 (7954) (2023) 813–816.
96. Z. Q. Yao, Y. Z. Xu, D. Binosi, Z. F. Cui, M. Ding, K. Raya, C. D. Roberts, J. Rodríguez-Quintero, S. M. Schmidt, Nucleon gravitational form factors, *Eur. Phys. J. A* 61 (5) (2025) 92.
97. Y.-Z. Xu, K. Raya, Z.-F. Cui, C. D. Roberts, J. Rodríguez-Quintero, Empirical Determination of the Pion Mass Distribution, *Chin. Phys. Lett. Express* 40 (4) (2023) 041201.
98. R. Aaij, et al., Updated measurements of exclusive  $J/\psi$  and  $\psi(2S)$  production cross-sections in  $pp$  collisions at  $\sqrt{s} = 7$  TeV, *J. Phys. G* 41 (2014) 055002.
99. U. Camerini, J. G. Learned, R. Prepost, C. M. Spencer, D. E. Wiser, W. Ash, R. L. Anderson, D. Ritson, D. Sherden, C. K. Sinclair, Photoproduction of the psi Particles, *Phys. Rev. Lett.* 35 (1975) 483.
100. B. Gittelman, K. M. Hanson, D. Larson, E. Loh, A. Silverman, G. Theodosiou, Photoproduction of the psi (3100) Meson at 11-GeV, *Phys. Rev. Lett.* 35 (1975) 1616.
101. W. D. Shambroom, et al., DIFFRACTIVE PRODUCTION OF VECTOR MESONS IN MUON PROTON SCATTERING AT 150-GEV AND 100-GEV, *Phys. Rev. D* 26 (1982) 1–22.
102. P. L. Frabetti, et al., A Measurement of Elastic  $J/\psi$  Photoproduction Cross Section at Fermilab E687, *Phys. Lett. B* 316 (1993) 197–206.
103. S. Aid, et al., Elastic electroproduction of  $\rho^0$  and  $J/\psi$  mesons at large  $Q^2$  at HERA, *Nucl. Phys. B* 468 (1996) 3–36, [Erratum: *Nucl.Phys.B* 548, 639–639 (1999)].
104. M. J. Amarian, Strangeness and charm production with HERMES, *Few Body Syst. Suppl.* 11 (1999) 359–362.
105. K. J. Eskola, C. A. Flett, V. Guzey, T. Löytäinen, H. Paukkunen, Predictions for exclusive  $\Upsilon$  photoproduction in ultraperipheral  $Pb + Pb$  collisions at the LHC at next-to-leading order in perturbative QCD, *Eur. Phys. J. C* 83 (8) (2023) 758.
106. J. Penttala, C. Royon, Gluon saturation effects in exclusive heavy vector meson photoproduction, *Phys. Lett. B* 864 (2025) 139394.
107. Y.-P. Xie, V. P. Gonçalves, Exclusive heavy vector meson photoproduction in  $pp$  and  $pPb$  collisions within the GPD approach: A phenomenological analysis – arXiv:2507.20448 [hep-ph].
108. K. Lukashin, et al., Exclusive electroproduction of phi mesons at 4.2-GeV, *Phys. Rev. C* 64 (2001) 059901.
109. C. Alexa, et al., Elastic and Proton-Dissociative Photoproduction of  $J/\psi$  Mesons at HERA, *Eur. Phys. J. C* 73 (6) (2013) 2466.
110. S. R. Klein, J. Nystrand, J. Seger, Y. Gorbunov, J. Butterworth, STARlight: A Monte Carlo sim-

ulation program for ultra-peripheral collisions of relativistic ions, *Comput. Phys. Commun.* 212 (2017) 258–268.

111. Y. Guo, X. Ji, Y. Liu, QCD Analysis of Near-Threshold Photon-Proton Production of Heavy Quarkonium, *Phys. Rev. D* 103 (9) (2021) 096010.